Redox Chemistry in Radiation Induced Dissolution of Spent Nuclear Fuel

- from elementary reactions to predictive modeling

Olivia Roth

KTH Chemical Science
and Engineering

KTH - Chemical Science and Engineering
Nuclear Chemistry
SE – 100 44 Stockholm
Sweden
2008

Doctoral Thesis in Chemistry

ISBN 978-91-7415-100-8
ISSN 1654-1081
TRITA-CHE Report 2008:60

Printed by Intellecta AB, Stockholm 2008

Abstract

The focus of this doctoral thesis is the redox chemistry involved in radiation induced oxidative dissolution of spent nuclear fuel and UO_2 (as a model substance for spent nuclear fuel).

It is shown that two electron oxidants are more efficient than one electron oxidants in oxidative dissolution of UO_2 at low oxidant concentrations. Furthermore, it is shown that H_2O_2 is the only oxidant that has to be taken into account in radiation induced dissolution of UO_2 under deep repository conditions (granite groundwater dominated by α-radiolysis). Previously determined rate constants for oxidation of UO_2 by H_2O_2 and O_2, and rate constants for dissolution of U(VI) from the surface are successfully used to reproduce numerous UO_2 dissolution rates reported in the literature.

The impact of reactive solutes (Fe(II)(aq), 2-propanol and chloride) and Pd-inclusions (as a model for ε-particles) in combination with H_2, on radiation induced oxidative dissolution of UO_2 is investigated. It is shown that both the studied reactive solutes (under oxygen free conditions) and the combination of Pd inclusions and H_2 inhibit the dissolution. Calculations (based on the fuel inventory) show that 1 μM Fe(II)(aq) decreases the dissolution rate by a factor of ~50 and that 1 ppm surface coverage of ε-particles is sufficient to completely stop the dissolution of 100 year old fuel (assuming 40 bar H_2).

The dissolution behavior of NpO_2 and PuO_2 in H_2O_2 containing aqueous solution without complexing agent is studied and compared to UO_2. Based on the measured dissolution rates, we would not expect the dissolution of the actinides to be congruent. Instead, in a system without complexing agent, the rates Np and Pu are expected to be lower than the U release rate.

The effect of ionizing irradiation on the UO_2 reactivity is studied in order to elucidate the effect of self-irradiation on the reactivity of the spent fuel matrix. It is shown that a threshold dose must be achieved before any effect of irradiation can be seen. Beyond the threshold the reactivity seems to increase with increasing dose. Furthermore, the effect appears to be permanent.

The effect of particle size on the reactivity of UO_2 powder is studied in view of proposed theories suggesting a particle size dependence of both the pre-exponential factor and the activation energy for redox reactions. The rate constant and activation energy for oxidation of UO_2 by MnO_4^- seems to agree with the proposed equations.

The radiation chemical synthesis of UO_2 nanoparticles is studied. It is shown that U(VI) released by dissolution of spent nuclear fuel could be reduced to UO_2 nanoparticles. These particles could, due to their high reactivity towards H_2O_2, act as oxidant scavenger in a future deep repository for spent nuclear fuel.

Sammanfattning

Denna doktorsavhandling behandlar redoxprocesser involverade i strålningsinducerad oxidativ upplösning av använt kärnbränsle och UO_2 (som modellsubstans för använt kärnbränsle).

Detta arbete visar att två-elektron oxidanter är mer effektiva än en-elektron oxidanter i oxidativ upplösning av UO_2 vid låga oxidantkoncentrationer. Dessutom visas, på kinetiska grunder, att H_2O_2 är den enda oxidant som måste tas hänsyn till vid stålningsinducerad oxidativ upplösning av UO_2 under djupförvarsförhållanden (granitiskt grundvatten dominerat av α-radiolys). Tidigare bestämda hastighetskonstanter för oxidation av UO_2 med H_2O_2 och O_2, samt hastighetskonstanter för upplösning av U(VI) från ytan har framgångrikt använts för att återskapa UO_2 upplösningshastigheter rapporterade i litteraturen.

Inverkan av reaktiva ämnen i vattenfas (Fe(II)(aq), 2-propanol och klorid) samt av Pd-inneslutningar (som modell av ε-partiklar) i UO_2 matrisen i kombination med H_2, på strålningsinducerad upplösning av UO_2 har studerats. Studien visar att både de reaktiva ämnena i vattenfasen (under syrefria förhållanden) och Pd- inneslutningar i kombination med H_2 hämmar upplösningen. Beräkningar (baserade på ett bränsleinventarie) visar att 1 μM Fe(II)(aq) minskar upplösningshastigheten med en faktor ~50 samt att 1 ppm ytbeläggning av ε-partiklar är tillräckligt för att effektivt stoppa uppslöningen av 100 år gammalt bränsle (vid 40 bar H_2).

Upplösning av NpO_2 och PuO_2, i jämförelse med UO_2, har studerats i vattenlösning innehållande H_2O_2 utan komplexbildare. Baserat på de uppmätta upplösningshastigheterna förväntas upplösningen av dessa aktinider från UO_2-bränsle vara inkongruent. I ett system utan komplexbildare kan NpO_2 odh PuO_2 upplösningshastighetern förvantas vara lägre än UO_2 upplösningshastigheten.

Effekten av joniserande strålning på reaktiviteten hos UO_2 har studerats för att klargöra effekten av egen-bestrålning. Studien visar att dosen måste nå ett visst tröskelvärde innan någon effekt på reaktiviteten kan observeras. Vid doser över tröskelvärdet ökar reaktiviteten med ökande dos. Effekten verkar vara permanent.

Partikelstorlekens inverkan på reaktiviteten hos UO_2 pulver har studerats med utgångspunkt i föreslagna samband mellan partikelstorlek och pre-exponentiell faktor och mellan partikelstorlek och aktiveringsenergi. Studien visar att hastighetskonstanten och aktiveringsenergin för reaktionen mellan UO_2 och MnO_4^- överenstämmer med de föreslagna sambanden.

Stålningskemisk syntes av UO_2 nanopartiklar har studerats. Studien visar att U(VI) frigjort genom upplösning av använt kärnbränsle i ett djupförvar kan reduceras till UO_2 nanopartiklar. Dessa partiklar kan, på grund av sin höga reaktivitet med H_2O_2, fungera som infångare av oxidanter i ett framtida djupförvar för använt kärnbränsle.

List of Papers

I. M. Jonsson, E. Ekeroth and O. Roth, Dissolution of UO_2 by one- and two electron oxidants, Mat. Res. Soc. Symp. Proc. 807 (2004) 77-82

II. E. Ekeroth, O. Roth and M. Jonsson, The relative impact of radiolysis products in radiation induced oxidative dissolution of UO_2, J. Nucl. Mater. 355 (2006) 38–46

III. O. Roth and M. Jonsson, Oxidation of UO_2(s) in aqueous solution, Cent. Eur. J. Chem. 6 (2008) 1–14

IV. O. Roth and M. Jonsson, On the impact of reactive solutes on radiation induced oxidative dissolution of UO_2, Submitted to J. Nucl. Mater.

V. M. Trummer, O. Roth and M. Jonsson, H_2 inhibition of radiation induced dissolution of spent nuclear fuel, Submitted to J. Nucl. Mater.

VI. M. Jonsson, F. Nielsen, O. Roth, E. Ekeroth, S. Nilsson and M.M. Hossain, Radiation induced spent nuclear fuel dissolution under deep repository conditions, Environ. Sci. Technol. 41 (2007) 7087-7093

VII. R. Pehrman, M. Amme, O. Roth, E. Ekeroth and M. Jonsson, Oxidative dissolution of actinide oxides in H_2O_2 containing aqueous solution, Submitted to J. Nucl. Mater.

VIII. O. Roth, S. Nilsson and M. Jonsson, Radiation enhanced reactivity of UO_2, J. Nucl. Mater. 354 (2006) 131–136

IX. O. Roth, T. Bönnemark and M. Jonsson, The influence of particle size on the kinetics of UO_2 oxidation in aqueous powder suspensions, J. Nucl. Mater. 353 (2006) 75–79

X. O. Roth, H. Hasselberg and M. Jonsson, Radiation chemical synthesis and characterization of UO_2 nanoparticles, Submitted to J. Nucl. Mater.

Comment on my contribution to the papers

In **Paper I**, I have performed the experiments and participated in the evaluation of data and to some extent in the preparation of the manuscript. In **Paper II**, I have performed around 50% of the experimental work, parts of the simulations and to a large extent participated in the planning of the experiment and the preparation of the manuscript.

For **Paper III**, I have done most of the literature collection and calculations and written parts of the manuscript. In **Paper IV** I have performed the experiments and simulations, contributed to a large extent to the planning and data evaluation and I have prepared the manuscript. For **Paper V**, I have participated in the planning of the experiments, the data evaluation and the preparation of the manuscript.

In **Paper VI** I have contributed with data, data evaluation and discussions concerning the manuscript.

In **Paper VII**, I have participated in the planning of the experiments, performed some experimental work and done major parts of the data evaluation and manuscript preparation.

In **Paper VIII** and **IX**, I have participated in the planning of the experiments and the data evaluation, performed some experiments and written major parts of the manuscripts. In **Paper X**, I have performed around 50% of the experimental work, participated in the data evaluation and prepared the manuscript.

Table of Contents

Introduction

Nuclear power is an important source of energy in Sweden and many other countries all over the world. In Sweden, nuclear power has been commercially used for energy production since 1963, when the Ågesta heavy water reactor was taken into operation [1]. Today, the future of nuclear power in Sweden is subject to intensive debate. One of the issues that have to be solved in order to maintain the nuclear power industry in a sustainable way is the management of the radioactive waste, in particular the spent nuclear fuel.

Regardless of which the future sources of energy will be, hazardous waste in the form of spent nuclear fuel has already been generated by the operation of nuclear power plants, and this waste has to be managed in a safe way. The spent nuclear fuel will have an increased level of radioactivity for a very long time and hence, needs to be isolated from the biosphere e.g. by placement in a geological repository. Sweden is in the international front line when it comes to designing a geological repository for spent nuclear fuel. The Swedish deep repository will be built according to the KBS-3 method based on a multi-barrier system, and is expected to be taken into use in 2018 [2,3].

Chemically, the geological repository is a very complex system involving interfacial processes and radiation chemistry. Numerous factors are affecting the chemical environment and these have to be thoroughly investigated in order to assess the safety of the deep repository. This makes the deep repository for spent nuclear fuel a challenging system to investigate, not only in terms of environmental protection, but also from a purely scientific point of view. One of the main issues in the safety assessment of a future deep repository is the rate of dissolution of the spent nuclear fuel matrix. This is also the focus of this thesis.

Background

In water-cooled nuclear reactors, the fuel normally consists of ceramic UO_2. After the use in a nuclear reactor, UO_2 is still the main component of the fuel, making up ~95 wt.% whereas the remaining 5% consist of fission products and heavier actinides [4,5]. Due to the content of radionuclides the spent nuclear fuel will have an increased level of radioactivity for around 100 000 years [6].

The Swedish spent nuclear fuel will be stored in a geological deep repository according to the KBS-3 method [2]. The deep repository will be built 500 m below ground level and the safety will be ensured by four barriers; the bedrock, a layer of bentonite clay, a copper canister and the UO_2-matrix of the fuel itself. Many of the radioactive species formed when burning the fuel in the reactor are incorporated in the UO_2-matrix and, if the outer barriers should fail and the fuel comes into contact with water, the release of most radionuclides is assumed to be controlled by the dissolution of the UO_2-matrix [7]. Under the reducing conditions expected at the depth of a geological repository, the matrix dissolution is slow, whereas the dissolution is significantly increased under oxidizing conditions [8]. When the fuel, in the case of barrier failure, is exposed to water, oxidizing species will be formed by radiolysis of water. This will alter the redox conditions in the deep repository and possibly undermine the barrier function of the UO_2-matrix.

The repository has been designed to fulfill some general principles, based on current legislation and on the public opinion. One of the principles is that very high safety is required, in both the short and long term perspective [2]. Hence, the political initiation of the construction of a deep repository needs to be based on a reliable long term safety analysis of the system. Given the long operational time span and the large number of processes involved, employment of numerical models and simulations, based on elementary reactions in the system, is necessary. As mentioned above, one of the key issues is the dissolution of the spent nuclear fuel matrix. Several attempts to numerically simulate the dissolution of spent fuel have been made [9-12]. Many of these simulations are, however, based on insufficient information about the kinetics and mechanisms for the surface reactions involved. Detailed information about these processes is a prerequisite for reliable modeling. Furthermore, detailed knowledge about the radiation chemistry and dose distribution in the aqueous phase surrounding the fuel is required.

Processes involved in oxidative dissolution of spent nuclear fuel have been subject to many studies [7,13]. In some of these studies pure UO_2 (sometimes in the form of UO_2 powder) has been used as a model substance for spent

nuclear fuel. However, the reactivity of pure UO_2 is not expected to be identical to the reactivity of spent nuclear fuel for a number of reasons. The reactivity will, for example, be affected by changes in physical properties due to in-reactor irradiation as well as by changes in chemical properties due to the presence of radionuclides.

Several studies using spent nuclear fuel have also been performed [7]. The fuel used in these studies is, however, relatively fresh and since the activity of the fuel as well as the relative importance of α-, β- and γ-radiation will change with time, these studies will not reflect future deep repository conditions. In systems involving spent nuclear fuel, there are several factors influencing the rate of dissolution. Hence, it is difficult to draw any conclusions regarding the kinetics and mechanisms for elementary surface reactions from this type of experiments alone.

The aim of this thesis is to investigate the redox chemistry involved in radiation induced oxidative dissolution of UO_2 and spent nuclear fuel. UO_2 and spent nuclear fuel are compared by elucidating some of the factors that differentiate UO_2 from spent nuclear fuel and how they influence the dissolution rate. Furthermore, the dissolution behavior of NpO_2 and PuO_2 (present in spent nuclear fuel) will, to some extent, be discussed and compared to the UO_2 dissolution behavior.

In the following sections some important processes occurring in a deep repository will be described – beginning with the production of oxidants by radiolysis of water, moving to heterogeneous reactions between aqueous species and the fuel surface, and finally the dissolution of the solid phase (UO_2 or spent nuclear fuel).

Radiation Chemistry of Water and Aqueous Solutions

Spent nuclear fuel emits α-, β- and γ-radiation. When such highly energetic (≥100 eV) radiation interacts with matter it gives rise to chemical changes. The energy of the radiation is very high compared to ionization energies (usually <15 eV) and to chemical bond energies (normally 1-5 eV) [14] and the interaction results in ionization of the irradiated material. Consequently, this type of radiation is frequently called ionizing radiation.

Ionizing radiation can be divided into two major groups; high-energy charged particles (e.g. He^{2+}, protons, electrons and positrons), neutrons and electromagnetic radiation of short wavelength (e.g. X-rays, bremsstrahlung and γ-radiation) [15]. A natural source of ionizing radiation is the decay of radioactive nuclei, which transform spontaneously and emit radiation. There are three main modes of nuclear decay; α-decay (emission of helium nuclei - He^{2+}), β-decay (emission of electrons or positrons) and γ-decay (emission of electromagnetic radiation).

When a material is irradiated it absorbs radiation energy. If the transferred energy is sufficiently high, it causes ionization of the atoms/molecules of the absorber, i.e. positive ions and electrons are produced. In most cases the energy of the ejected electron is high enough to cause secondary ionizations of the material. In interactions where the transferred energy is too low to ionize the material the radiation may instead cause excitation of the atoms. The total radiation energy absorbed by the irradiated material is called the *absorbed dose* (D). The SI unit is *Gray* (1 Gy=1 J kg^{-1}). The *dose rate* is the absorbed dose per unit time (Gy s^{-1}) [16].

The mechanism for energy absorption depends on the type of radiation. Heavy, highly charged particles (i.e. He^{2+}) interact strongly with the absorbing medium. Hence, the penetration depth is short and the energy is deposited in a small volume of the absorber. Due to the high particle mass the deflection caused by interacting coulomb fields is small, leading to straight paths. Furthermore, the produced secondary electrons have relatively low energy and only a minor part of them cause secondary ionization [14,16].

Lighter, less charged particles (i.e. electrons) have longer penetration depths and are more widely scattered out of the incident beam path. The secondary electrons have higher energy (compared to secondary electrons from e.g. α-absorption) and in β-absorption 70-80% of the total ionization is caused by the secondary electrons. Electromagnetic radiation (i.e. γ-photons) interacts very sparsely with the absorber due to the absence of charge and mass. Consequently, the penetration depth is much longer and all the energy is lost in one or a few interactions. The ionization caused by γ-absorption is almost

completely due to secondary ionization. The absorption of energy from charged particles is described by LET-values (*linear energy transfer*), which are defined as the energy absorbed per unit length of matter [14,16].

The ionized or excited species formed as a result of the energy transfer are located to spurs in the absorber. The spurs are more sparsely or densely packed depending on the absorption mechanism. Heavy, charged particles give rise to closely located spurs, whereas lighter, less charged particles or photons give widely spread spurs. The distribution of the spurs affects the final yields of the radiolysis products. The *radiation chemical yield* is described in terms of G-values, which are the number of moles of the irradiated material transformed per Joule of absorbed energy (mol J^{-1}) [14,16].

When pure water is irradiated, H_2O^* (excited water molecule) can be formed, or when the radiation energy is high enough, the water decomposes into H_2O^+ and e^-. Through spur reactions a number of reactive radicals and molecular species are produced. The yields of radiolysis products in water exposed to fast electrons, γ- or α- radiation are given in Table 1. The yields depend on the type of radiation due to the differences in spur distribution. When the spurs are densely packed (as for α-radiation) recombination reactions will be favored, leading to lower radical yields and, consequently, higher yields for the molecular products [14].

When dilute (<0.1 M) aqueous solutions are irradiated, practically all the deposited energy is absorbed by the water molecules and the primary yields of the radiolysis products will be unaffected. The final product yield is however changed by chemical reactions between solutes and the products of water radiolysis [14].

In a future deep repository for spent nuclear fuel, solutes (e.g. carbonate, organic substances and salts) present in natural groundwaters will affect the generation of radiolysis products. For example, carbonate present in the water reacts with $OH^\bullet$ according to reaction 1. In Swedish groundwater, containing 2-10 mM carbonate [17], $OH^\bullet$ will be quantitatively converted to $CO_3^{\bullet-}$.

$$OH^\bullet + HCO_3^- \rightarrow H_2O + CO_3^{\bullet-} \quad (1)$$

Table 1. Product yields (G-values) in irradiated neutral water [14].

Radiation	**G (H_2O)** μmol J^{-1}	**G (H_2)** μmol J^{-1}	**G (H_2O_2)** μmol J^{-1}	**G (e_{aq}^-)** μmol J^{-1}	**G ($H^\bullet$)** μmol J^{-1}	**G ($OH^\bullet$)** μmol J^{-1}	**G ($HO_2^\bullet$)** μmol J^{-1}
γ and fast e^-	-0.43	0.047	0.073	0.28	0.062	0.28	0.0027
12 MeV α	-0.294	0.115	0.112	0.0044	0.028	0.056	0.007

Addition of solutes can also be used in laboratory experiments to control the yield of specific radiolysis products. An example of this is the use of nitrous gas which scavenges the solvated electron and forms $OH^{\bullet}$ (reaction 2). Another example is addition of oxygen, which will favor the production of superoxide according to reaction 3.

$$e_{aq}^- + N_2O(aq) + H_2O \rightarrow OH^{\bullet} + OH^- + N_2 \quad (2)$$

$$O_2 + e_{aq}^- \rightarrow O_2^{\bullet -} \quad (3)$$

Reducing conditions can be obtained by adding secondary alcohols e.g. 2-propanol. The secondary alcohol reacts with both $OH^{\bullet}$ and $H^{\bullet}$ forming a strongly reducing radical according to reaction 4 [18].

$$H_3C\text{-}CHOH\text{-}CH_3 + OH^{\bullet}\ (H^{\bullet}) \rightarrow (CH_3)_2\text{-}C^{\bullet}OH + H_2O\ (H_2) \quad (4)$$

In a heterogeneous system, energy, charge and matter can be transported through the interface. This, as well as catalytic and steric effects, could alter the water decomposition. In radiation induced oxidative dissolution of spent nuclear fuel, the central reaction is the reaction between radiolysis products formed in the water surrounding the fuel and the fuel surface. Hence, it is of crucial importance to elucidate the effects of the presence of a solid surface on the yield of water radiolysis products.

LaVerne *et. al.* [19-22] have studied the radiolytic H_2 production in the presence of solid oxide surfaces. Some of these experiments were performed on thin films of water on the oxide surface, others on powder suspensions or slurries. These studies show that, in general, the G-value increases with decreasing number of water layers on the surface. The rationale for this is probably that energy originally deposited in the solid phase is transferred to the liquid phase. The effect clearly depends on type of oxide and surface morphology.

Experiments performed on slurries and suspensions show that very high solid surface area to solution volume ratios are required to significantly increase the G-value for H_2 above that of bulk water [20]. For SiO_2 in water a surface area to solution volume ratio of ~10^7 is required to observe an effect on the G-value [20]. This corresponds to a water layer with a thickness of ca 60 nm, i.e. significantly lower than the maximum range of α-particles. The surface area to solution volume ratio in dissolution of spent nuclear fuel in aqueous solution is several orders of magnitude lower than 10^7. Hence, the surface enhanced H_2 production will not be important in this system.

Radiolytic production of H_2O_2 does not appear to be affect by the presence of oxide surfaces to the same extent as H_2 [19].

Heterogeneous Reactions and Reactivity of Nanoparticles

Oxidative dissolution of UO_2 and spent nuclear fuel takes place by heterogeneous reactions, i.e. reactions at the solid liquid interface. This type of process can be divided into the following steps:

1. Transport (diffusion) of the reactants in solution to the surface
2. Adsorption of the reactants on the surface
3. Surface diffusion of reactants
4. Reactions on the surface
5. Desorption (dissolution) of products
6. Transport (diffusion) of products away from the surface

Any of these steps may be rate determining [23]. There are several reasons why the rate of a heterogeneous reaction differs from the rate of the analogous reaction in a homogeneous phase. One important factor is the decreased mobility of one of the reactants in the heterogeneous system.

Generally, the rate of a chemical reaction depends on the concentration of reactants and the rate constant for the reaction. For a reaction between a solute and a solid reactant, two rate expressions can be derived; Eq. 5 describing the rate of solute consumption and Eq. 6 describing the rate of surface reaction. In these equations *SA* denotes the solid surface area, *V* the volume and *k* the rate constant for the reaction between the solute and the surface.

$$-\frac{d[Solute]}{dt} = k\left(\frac{SA}{V}\right)[Solute] \tag{5}$$

$$-\frac{dn_{Solid}}{dt} = k(SA)[Solute] \tag{6}$$

In practice, the normal procedure for determining second order rate constants in heterogeneous systems is to monitor the concentration of solute reactant as a function of reaction time. When an excess of solid material is used, the reaction will be of pseudo-first order, and the pseudo-first order rate constant can be obtained from the slope when plotting the logarithm of the solute reactant concentration versus time. By repeating this procedure for a number of different solid surface area to solution volume ratios, the second order rate constant can be determined from the slope when plotting the pseudo-first order rate constant as a function of surface area to solution

volume ratio. Since the surface area to solution volume ratio has the unit m^{-1}, the unit for the second order rate constant of the heterogeneous reaction is m s^{-1}. When performing this type of experiments the use of powder suspensions is convenient, providing large surface area to volume ratios and large flexibility of the system.

The rate constant can be expressed by the empirically derived Arrhenius equation:

$$k = Ae^{\frac{E_a}{RT}} \tag{7}$$

where R is the universal gas constant, T the temperature and E_a the activation energy of the reaction. The parameter A is referred to as the pre-exponential factor.

Similar expressions for the rate constant can be theoretically derived from transition state theory (Eyring equation) [24]. The pre-exponential factor in the Arrhenius equation can be interpreted as the collision frequency between the reactants. Both transition state theory and collision theory predict a temperature dependence of the pre-exponential factor [24]. This is not accounted for in the Arrhenius equation and can also be neglected in many practical implementations within reasonable temperature intervals.

For reactions with low activation energy, the exponential term in Eq. 7 approaches one and the rate constant is determined by the pre-exponential factor. In this case the rate of the reaction is controlled by the rate of molecular encounters or more specifically, by the diffusion of the reacting species in the system. Hence, the pre-exponential factor is sometimes referred to as the diffusion controlled rate constant and can be interpreted as the highest possible rate of reaction since reaction occurs in each encounter.

The diffusion limit for a heterogeneous system differs significantly from a homogeneous system. In a homogeneous system of two uncharged dissolved molecules, A and B, the diffusion controlled rate constant can be calculated by Eq. 8, derived from Fick's first law [24]:

$$k_{diff} = 4\pi(D_A + D_B)(R_A + R_B) \tag{8}$$

D_A and D_B refer to the diffusion coefficients of the reactants, R_A and R_B to the molecular radii. The diffusion coefficient is (approximately) related to the radius of the molecule by the Stoke-Einstein relationship [24]:

$$D_A = \frac{k_B T}{6\pi\eta \times R_A} \tag{9}$$

where k_B, T and η denote the Boltzmann constant, the temperature and the viscosity of the solvent.

By substituting this expression into Eq. 8, the diffusion controlled rate constant for a homogeneous reaction can be expressed by:

$$k_{diff} = \frac{2k_B T}{3\eta} \times \frac{(R_A + R_B)^2}{R_A \times R_B} \tag{10}$$

A heterogeneous system, where a solute reacts with a solid reactant, can be described using a model where the active sites of the solid reactant are localized on the surface of solid, spherical particles with radii significantly larger than the molecular radii of the reactants. Employing basic collision and diffusion theory the reaction rate in such a heterogeneous system can be described by Eq. 11 [25].

$$\frac{d[Solute]}{dt} = -\frac{2k_B T}{3\pi\eta} \frac{R_{Solid}^2}{R_{Solute} R_p} \left(e^{-\frac{E_a}{RT}} \right) [Solute] \frac{N_{Solid(surf)}}{V} \tag{11}$$

where $[Solute]$ denotes the concentration of reactant in solution, R_{Solute} and R_{Solid} are the molecular radii of the solute and the solid material, respectively. $N_{Solid(surf)}$ denotes the number of solid phase molecules on the particle surface being exposed to the solution of volume V. R_p denotes the radius of the solid particles. As can be seen from this equation, the diffusion controlled rate constant increases with decreasing particle size.

Using Eq. 10 and 11, the ratio between the diffusion controlled rate constants in the homogeneous and heterogeneous case (of the same reaction) can be derived;

$$\frac{k_{Het}}{k_{Hom}} = \frac{R_{Solid}^3}{\pi \times R_p (R_{Solute} + R_{Solid})^2} \tag{12}$$

The ratio is clearly much smaller than one, indicating that the heterogeneous reactions should be significantly slower than its homogeneous analogue [25].

Not only the pre-exponential factor but also the activation energy can differ between the heterogeneous and homogeneous case, e.g. due to changes in potential energy surface of the reaction [25]. For nanometer-sized materials it is well known that the activation energy depends on the particle size due to

quantum mechanical effects [26-28]. The energy levels in small particles approach those of single molecules. In bulk material, the energy levels are continuously distributed, whereas in single molecules they are discrete. When decreasing the particle size, the levels of the valence band are moderately shifted to lower energies, while there is a strong shift to higher energies for the conduction band [29]. Hence, the quantum mechanical effect gives rise to a broader band gap between the valence band and the conduction band in small particles compared to the bulk material, which would lead to higher activation energy for oxidation of small particles. This is not obvious for larger particles. However, it has been suggested that the activation energy for electron transfer reactions should depend on the particle size according to Eq. 13 [30].

$$-\Delta E_a = k_B T \ln \frac{N_{Solid(surf)}}{N_{Solid(bulk)}} = k_B T \ln \frac{1}{R_p} \qquad (13)$$

This equation originates from the simple fact that larger particles contain more electrons than smaller particles relative to the number of surface sites (the electron content increases with R_p^3 while the number of surface sites increases with R_p^2) and that a large pool of electrons would lower the energy barrier for removal of electrons. Hence, the activation energy should decrease with increasing particle size. Using the Boltzmann distribution Eq. 13 is obtained, where $N_{Solid(surf)}$ and $N_{Solid(bulk)}$ denote the number of molecules on the surface and the molecule content of the particle, respectively.

When substituting the activation energy in Eq. 11 for the expression in Eq. 13 we find that the particle size (R_p) is cancelled from the equation. That is, the particle size effect on the pre-exponential factor and the activation energy cancel each other completely. Hence, on the basis of these equations we can expect no effect on the rate constant from a change in particle size.

In the complete rate expression for solutes reacting with solid spherical particles (Eq. 11), the amount of solid molecules on the surface being exposed to the solution ($N_{Solid(surf)}$) appears as a measure of the amount of solid reactant. This is very difficult to quantify and the solid surface area is often used instead. The surface area obtained by BET measurements is frequently used. It is, however, not obvious that the BET surface area is an adequate measure of the true surface area available to reactants in the solution. This, and the non-spherical geometry of particles used in experiments, makes it impossible to calculate the exact theoretical diffusion controlled rate constant for a real system. The order of magnitude can nevertheless be estimated.

Oxidation and Dissolution of UO_2

Even though the redox chemistry of UO_2 is of great importance in uranium mining, manufacturing of nuclear fuel, reprocessing and geological deposition of spent nuclear fuel, there are relatively few quantitative studies on the kinetics of UO_2 oxidation in aqueous solution. Oxidation of UO_2 significantly increases the solubility and is the main route to dissolution in most applications of practical importance. The process can be described by two reactions (14) oxidation of UO_2 and (15) dissolution of oxidized UO_2 from the surface:

$$U(IV)(s) + Ox \rightarrow U(VI)(s) + Red \quad (14)$$

$$U(VI)(s) \rightarrow U(VI)(aq) \quad (15)$$

Reaction 15 is significantly enhanced by the presence of complexing agents in the aqueous phase e.g. $HCO_3^{\bullet}$ [31]. The rate constants for $HCO_3^{\bullet}$-facilitated dissolution of U(VI) from the surface and the corresponding reaction in pure water has been determined to $\sim 10^{-6}$ m s^{-1} and $7 \pm 1 \times 10^{-8}$ mol m^{-2} s^{-1} respectively [32].

The oxidation reaction (reaction 14) requires the transfer of two electrons, either to a two-electron oxidant e.g. H_2O_2 or to two molecules of a one-electron oxidant e.g. $OH^{\bullet}$. The mechanism for oxidation is expected to differ between the two types of oxidants according to the following scheme:

Two electron oxidant:

$$U(IV)_{surf} + 2\text{-}e^- \, Ox \rightarrow U(VI)_{surf} + 2\text{-}e^- \, Red \quad (16)$$

One-electron oxidant:

$$U(IV)_{surf} + 1\text{-}e^- \, Ox \rightarrow U(V)_{surf} + 1\text{-}e^- \, Red \quad (17)$$

$$U(V)_{surf} + 1\text{-}e^- \, Ox \rightarrow U(VI)_{surf} + 1\text{-}e^- \, Red \quad (18)$$

$$U(V)_{surf} + U(V)_{surf} \rightarrow U(IV)_{surf} + U(VI)_{surf} \quad (19)$$

When no U(VI)-complexing agent is present (and the pH is high), an oxidized layer will build up on the surface [33-36]. The stoichiometry of the secondary phase depends on the conditions (type of oxidant and concentration) [37,38]. The formation of an oxidized layer will decrease the surface area available to the oxidant and eventually, the oxidation rate will be completely controlled by

the rate of dissolution of U(VI) from the surface. Consequently, it is difficult to study oxidation kinetics without the influence of dissolution

Numerous electrochemical studies have been performed on the corrosion of UO_2 [7]. In general, the corrosion current (corresponding to the corrosion rate) is determined as a function of corrosion potential. By determining the corrosion potential as a function of concentration of different oxidants, relationships between the oxidant concentration and the corrosion current, and thereby the rate of oxidation, can be derived.

By determining the rates of UO_2 dissolution in the presence of various oxidants (having different reduction potentials) and comparing these dissolution rates to the ones obtained when applying an external overpotential to the material, Nicol and Needes [39,40] showed (in 1975) that the rate of dissolution of UO_2 in acid as well as in carbonate media is determined by an electrochemical reaction i.e. electron transfer. Their studies also include quantification of the effects of various additives such as sulphate, sulphide and phosphate and the effects of pH, temperature and carbonate concentration. Furthermore, the authors developed an electrochemical model describing the UO_2 dissolution as a function of experimentally determined Tafel slopes which was found to agree well with experimental data.

The electrochemical nature of the UO_2 dissolution reaction has also been shown more recently by Shoesmith *et. al.* [41], who also used a similar electrochemical model to describe the impact of O_2 and H_2O_2 on the dissolution of UO_2. Shoesmith *et. al.* [41] propose that the oxidation of the UO_2 surface proceeds in two steps; (1) at low potentials - oxidation to $UO_{2.33}$ with the fluorite structure intact and low dissolution ("chemical dissolution") (2) at higher potentials - further oxidation to $UO_{2.67}$ with distortion of the fluorite structure and accelerating dissolution ("oxidative dissolution"). The threshold potential is suggested to be -100 mV vs. SCE. The authors claim that the dissolution rate, being first-order dependent on oxidant concentration at high concentrations, rapidly decreases as the threshold is approached. For H_2O_2, a region where the dissolution rate is independent of oxidant concentration is also suggested.

Numerous studies, both electrochemical and other, on the influence of pH, temperature, oxidant concentration, carbonate and other potential groundwater species have also been performed [7]. In most of these studies, the experiments are optimized to obtain rates of dissolution rather than rate constants for oxidation or dissolution. This often results in system specific rates or rate expressions that are dependent on the experimental conditions and not always applicable to other systems.

For this reason it is desirable to obtain rate constants for elementary reactions as they are not system specific. The rate constant for oxidation of

UO_2 has been determined for some different oxidants; $Fe(EDTA)^-$, H_2O_2, MnO_4^- and $IrCl_6^-$, in aqueous solution without added U(VI)-complexing agent [42]. The logarithm of the rate constants were found to be linearly related to the one-electron reduction potential of the oxidant. This enables prediction of rate constants for other oxidants and also led to the conclusion that the first electron transfer is the rate determining step in the oxidation. However, since no complexing agent was present, these rate constants will be affected by the rate of U(VI) dissolution from the surface and can not be regarded as the true rate constants for the oxidation reaction, the relative trend should nevertheless be valid. The reaction between H_2O_2 and UO_2 has been studied in systems containing HCO_3^- [32]. It was found that at carbonate concentrations above 1 mM, the second order rate constant was independent of HCO_3^- concentration, which enabled determination of the accurate rate constant for the oxidation reaction – 7.3×10^{-8} m s^{-1}. Values, within the same order of magnitude, have been reported in other publications [43,12].

Both O_2 and H_2O_2 are capable of multiple electron transfer. Consequently, the oxidation of UO_2 by these oxidants will be a stepwise process in which the first single electron transfer is rate limiting. The mechanism for oxidation of UO_2 by H_2O_2 is described by reaction 20 and 21.

$$H_2O_2 + UO_2(s) \rightarrow OH^\bullet + OH^- + UO_2^+ (s) \quad (20)$$

$$OH^\bullet + UO_2^+(s) \rightarrow OH^- + UO_2^{2+}(s) \quad (21)$$

Oxidation of UO_2 by O_2 takes place by a simple electron transfer mechanism. Judging from the relationship between rate constant and one-electron reduction potential [42], H_2O_2 is approximately 200 times more reactive towards UO_2 than O_2. This is in good agreement with electrochemical observations and values of the rate constant between UO_2 and O_2 reported in the literature [44,45]. Rate constants for oxidation of UO_2 by water radiolysis products are summarized in Table 2 (page 19).

Dissolution of Spent Nuclear Fuel

Radiation induced dissolution

As mentioned earlier, the kinetics for dissolution of spent nuclear fuel is expected to differ from that of unirradiated UO_2. The differences arise mainly because of the presence of fission products and transuranium elements formed when using the fuel in a nuclear reactor. Some important processes involved in dissolution of spent nuclear fuel are shown in Fig. 1.

The oxidants will in this case be produced by radiolysis of water, caused by the inherent radioactivity of the spent fuel. The oxidizing species (e.g. O_2, H_2O_2, $OH^{\bullet}$) will react with U(IV) on the fuel surface, forming U(VI). When carbonate is present in the groundwater, as expected in a Swedish deep repository [17], U(VI) will be effectively dissolved and removed from the surface. As the UO_2-matrix is dissolved, fission products and actinides are released into the solution. Thus, the rate of oxidant production at the fuel surface is of crucial importance in the estimation of spent fuel dissolution kinetics. The oxidant production rate is a function of the dose rate, which in turn is a function of the radionuclide content in the fuel (varies with fuel age and burn-up). A model describing the geometrical dose distribution (dose as a function of distance from the fuel surface) on the basis of radionuclide inventory have been developed recently [46].

The dose decreases dramatically with increasing distance from the fuel, introducing a gradient in the rate of water radiolysis [46]. Hence, diffusion as well as surface reactions and homogeneous reactions in the aqueous phase must be taken into account when determining the surface concentration of oxidants. Consequently, a rather complicated set of reactions is needed to calculate the rate of spent fuel matrix dissolution. The complexity can however be reduced to some extent by the following boundary conditions; the rate of UO_2 dissolution can never exceed the rate of UO_2 oxidation and the rate of oxidant consumption can never exceed the rate of oxidant production. When the rate of oxidant consumption is equal to the rate of radiolytic oxidant production, the system is in steady-state. This corresponds to the maximum rate of reaction between oxidants and the UO_2 surface and consequently, also to the maximum dissolution rate.

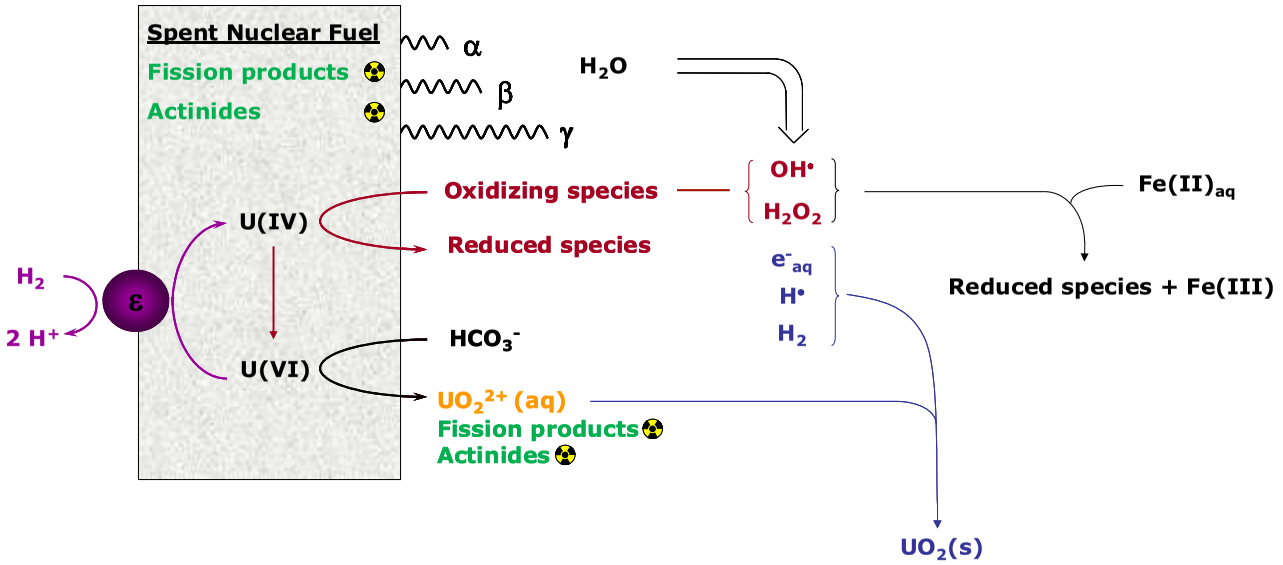

Figure 1. Schematic picture of important processes involved in radiation induced oxidative dissolution of spent nuclear fuel.

If the removal of U(VI) from the surface is efficient, the surface area available for reductants becomes very small and the direct reduction of U(VI) will be of minor importance. There are however cases when the reductants have to be taken into account. Among the reducing species formed by radiolysis of water, $H^{\bullet}$ and e_{aq}^- will only be present in very low steady-state concentrations. H_2 will be present in higher concentrations (produced both radiolytically and by corrosion of the iron insert of the canister containing the spent fuel), but is much less reactive and often requires a catalyst. Nevertheless, experimental studies have shown that H_2 has a significant suppressing effect on the dissolution of spent nuclear fuel [47,48].

There are three ways in which the presence of H_2 could lower the amount of dissolved U(VI) in solution; (1) by reacting with the radiolytically produced oxidants, reducing the oxidant concentration and thereby the UO_2 dissolution rate, (2) by reacting with dissolved U(VI) (this would however, not reduce the rate of spent fuel dissolution and does not explain the observed decrease in fission product release), (3) reduction of U(VI) in the solid phase or at the fuel surface. It has been suggested that the solid phase/surface reduction can be catalyzed by nanometer-sized noble metal particles present in the spent nuclear fuel [49]. These particles are often referred to as ε-particles and consist of alloys of metallic fission products (Mo, Pd, Ru, Tc and Rh) [50]. If this process takes place at the same rate as the oxidation, it would effectively inhibit the dissolution of the UO_2 matrix. The reaction between H_2 and radiolytic oxidants is probably also catalyzed by ε-particles but is nevertheless to slow to have any significant impact on the spent fuel dissolution rate [51].

Electrochemical experiments performed on UO_2 doped with synthetic ε-particles showed a significant decrease in corrosion potential in the presence of H_2 [49]. Recently, experiments performed on Pd-doped UO_2 in aqueous H_2O_2 solution under H_2 atmosphere showed that the rate of UO_2 dissolution decreased with increasing amount of Pd and with increasing H_2 pressure [52] (see Table 2). The kinetics for the process was found to be close to diffusion controlled. These findings have been used in estimations of the dissolution rate of spent nuclear fuel with different inventories and found to agree well with experimental results [53,54].

Apart from these surface processes, bulk reactions affecting the oxidant concentration could also be of importance. For example, Fe(II)(aq) (produced by canister corrosion) will reduce the amount of oxidants in the system. In reducing parts of the system, U(VI) dissolved from the surface can be reduced to U(IV). This process could lead to the formation of UO_2 particles, which might act as oxidant scavengers.

Table 2. Rate constants for oxidation of UO_2 by the products of water radiolysis [32,42] and for the solid phase/surface reduction of UO_2^{2+} catalyzed by Pd [52].

	O_2	H_2O_2	$OH^{\bullet}$	$CO_3^{\bullet-}$	$O_2^{\bullet-}$	$HO_2^{\bullet}$	H_2 (Pd)
	m s^{-1}	m s^{-1}	m s^{-1}	m s^{-1}	m s^{-1}	m s^{-1}	m s^{-1}
UO_2/UO_2^{2+}	3.9×10^{-10}	7.3×10^{-8}	1×10^{-6}	1×10^{-6}	1.8×10^{-9}	6×10^{-6}	1×10^{-6}

Factors influencing the fuel matrix reactivity

The use of the fuel in a reactor and the presence of impurities in the form of fission products and actinides may also influence physical properties, such as the electric conductivity, surface structure etc., that are important for the reactivity of the material.

The solid-state radiation effects on the UO_2 crystal structure appear however, to be relatively minor. During the in-reactor burning process the high temperature will cause annealing of the fuel and any limited effects that occur will be mitigated. However, when removing the fuel from the reactor the temperature will progressively decrease and the propensity for radiation damage increases and at ambient temperature, UO_2 can be slightly damaged e.g. by α-particles and electrons [4]. Irradiation of UO_2 with ≥1.8 MeV electrons has also been shown to induce minor defects in crystal structure [55].

During in-reactor irradiation, the steep thermal gradient in the fuel and the low strength of the UO_2 result in cracking of the material, leading to increased surface area of the fuel. The burning process also affects properties such as grain structure, grain size and porosity, which are likely to affect the reactivity and the dissolution rate [4]. At high fuel burn-ups (>45 GWd tU^{-1}) a porous outer ring is formed on the surface of the fuel (so called rim-effect and cauliflower structure). The mechanism behind this effect is unknown. The zone is typically 100 to 200 μm thick and accounts for ~4 to 8% of the fuel volume and is characterized by high porosity (up to 30%), large reduction in grain size (0.5-2 μm) and high radioactivity content (~10% of the inventory of the fuel) [56,57].

UO_2 with slight excess of oxygen (present as O^{2-}) exhibit semiconducting properties due to the formation of U(V) and U(VI). The higher oxidation states create positive holes in the U5f band. The holes can migrate by a hopping mechanism, where the normally localized electrons move from one cation to the next in a series of thermally activated jumps with low activation energy (~0.2 eV) [5]. The conductivity is strongly dependent on purity, apparent density and defects in crystalline structure. The history (e.g. sintering) and the temperature of the UO_2 are other factors that strongly influence its electrical properties [58]. Increased electrical conductivity involves increased mobility of electrons, which would facilitate electrochemical reactions.

Due to the radionuclide content the spent nuclear fuel will be exposed to continuous self-irradiation. The energy deposited in the material due to self-irradiation could possibly raise electrons to the valence band and hence contribute to increased electrical conductivity. Furthermore, substitution of

trivalent fissions products (e.g. Y^{3+}, La^{3+} and Nd^{3+}) for U(IV) requires further oxidation to maintain the charge balance and thereby contributes to the formation of positive holes in the matrix and consequently, increased electrical conductivity [59]. However, recent results, presented by He *et. al.* [60], indicate that the structural changes occurring from the incorporation of fission products decreases the UO_2 dissolution rate.

Although UO_2 constitutes, in terms of mass, the majority of the spent nuclear fuel material, its main radiotoxicity is (after extended storage times) contained in actinides with half lives shorter than that of 238-uranium, such as isotopes of Np and Pu. The rates of Np and Pu dissolution from spent nuclear fuel have been determined [61,62]. However, experiments aiming at understanding the radiolytic dissolution kinetics of the homogeneous phases NpO_2 and PuO_2 can not be found in the open literature. Especially in the case of Pu, it is not clear if its dissolution in radiolytic environments is controlled by the reaction with products of water radiolysis or by other mechanisms. Some authors have found evidence that radiolysis products may be of importance [63].

In general, Np and Pu are significantly less studied than U, due to their extremely low natural abundance and higher radiotoxicity, which makes experiments more expensive and more hazardous to perform. However, some trends and similarities in properties of the different actinides can be noted. The most stable oxidation state in aqueous solution changes from VI in the case of U, to V for Np and IV for Pu and it can be noted that the one-electron reduction potential of the AnO_2^+ ion increases in the order U<Np<Pu [64]. In the hexavalent oxidation state they all form AnO_2^{2+} ions [9]. The acidity of the actinyl ions decrease in the order $UO_2^{2+} > NpO_2^{2+} > PuO_2^{2+}$ [65], which indicates that the solvation energy decreases in the same order. Ions of all three actinides are known to form strong complexes with inorganic anions such as SO_4^{2-} and CO_3^{2-} [65]. The stability of these complexes mainly depends on the oxidation state and should be similar for the three actinides [65].

All three actinides are also known to form solid peroxo complexes and there are indications that the Pu peroxo complexes are less stable at room temperature than the corresponding Np and U complexes [66,67]. In groundwaters with low concentrations of complexing agents these complexes could potentially control an incongruent dissolution scheme of Np / Pu and the UO_2 matrix during the spent fuel dissolution reaction [68].

The lack of information about the effects of the radiolytic environment on the oxidation states of Np and Pu, as well as the ability of peroxo ligands to form complexes with actinide/actinyl ions in solution, complicate predictions of their actual behavior. Although Np and Pu, as higher homologues of U in

the actinide series of elements, let expect parallels of their dissolution behavior with that of uranium, it seems improbable that they will display identical oxidation and dissolution kinetics. Such differences may result in an incongruent dissolution from the spent nuclear fuel matrix under radiolytic conditions and deserve attention. This is increasingly important when considering long term deposition of MOX fuel and UO_2-fuel with higher burn-up.

Experimental Details

Most of the experiments performed involve the study of reactions between a solid reactant and reactants in the aqueous phase. The solid materials used were UO_2 powder (~8 μm), UO_2 pellets (with and without Pd), fragments cut from UO_2 pellets, UO_2 nanopowder (~30 nm) and powders of NpO_2 and PuO_2. In all the studies were UO_2 was used, it was washed with 10 mM HCO_3^- prior to the experiments in order to remove U(VI) from the surface. In all studies using powder suspensions, the samples were filtered before analysis.

The following instruments and analytical methods have been used:

- Jasco V-530 UV/VIS-Spectrophotometer, WPA lightwave S2000 Biochrom and Lovibond PCCheckit photometer for UV/visible spectroscopy.

- U(VI)(aq) concentrations were measured by Scintrex UA-3 Uranium Analyser [69], ICP-OES (Varian Vista Ax) or spectrophotometrically at 420 nm or at 653 nm using the Arsenazo(III) method [70,71].

- Np(aq) and Pu(aq) concentrations were measured by ICP-MS ThermoFinnigan Element 2 (ThermoFinnigan, Bremen, Germany).

- H_2O_2 concentrations were measured indirectly by UV/visible spectroscopy using I_3^- (360 nm) [72-74] or DPD (*N*,*N*-diethyl-1,4-phenylene diammoniumsulfate, 528 nm) [75,76] as an indicator.

- MnO_4^- and $IrCl_6^{2-}$ concentrations were measured by UV/visible spectroscopy at 545 nm and 488 nm respectively.

- Microtron electron accelerator (electron energy 6-6.5 MeV, pulse duration 4 μs) Pulse frequency; 12.5, 25 and 50 Hz. Dose rate at 12.5 Hz: ~24 Gy s^{-1} (corresponding to ~10^8 Gy s^{-1} in the pulse) determined by Fricke dosimetry [14].

- Co-60 γ-source with dose rate of ~0.06 Gy s^{-1} (determined by Fricke dosimetry [14]).

- Cs-137 γ-source with dose rate of ~0.15 Gy s^{-1} (determined by Fricke dosimetry [14]).

- BET equipment (Micromeritics Flowsorb II 2300 with 30% N_2 in Helium).

- Photon correlation spectroscopy (PCS) using a BI-90 particle sizer, Brookhaven Instruments Co, USA with wavelength 488 nm and fixed scattering angle 90°.

- Scanning Electron Microscopy.

Detailed information of each experiment is found in the publications.

Oxidative dissolution of UO_2 by one- and two-electron oxidants (Paper I)

In order to compare the efficiency between one- and two-electron oxidants in dissolving UO_2, dissolution yields were measured for the reaction between UO_2 and two different oxidants at different initial oxidant concentrations. The oxidants used were $IrCl_6^{2-}$ (one-electron oxidant) and H_2O_2 (two-electron oxidant). In all experiments aqueous suspensions of 0.2 g UO_2 powder in 20 mL 10 mM HCO_3^- solution, were used. The suspensions were purged with Ar throughout the experiments and stirred by a magnetic stirrer. Controlled amounts of oxidant were added to the aqueous suspensions and were allowed to be completely consumed before sampling.

For each experiment a reference experiment with identical conditions (and time) but without added oxidant was performed and used for background correction.

The relative impact of radiolysis products in radiation induced oxidative dissolution of UO_2 (Paper II)

In this investigation, the relative impact of radiolytically formed oxidants on UO_2 dissolution was studied. This was done by analyzing the amount of dissolved U(VI) as a function of time in 10 mL Co-60 γ-irradiated aqueous 10 mM HCO_3^- solutions containing a UO_2-pellet. In order to favor the formation of different oxidizing species (according to reaction 2-3) in the system the conditions were varied by saturating the solutions with different gases or gas-mixtures: Ar, N_2O, O_2, air and N_2O/O_2 (80/20 mol%). Samples were taken regularly during ~70 minutes irradiation and the U(VI) concentration of each sample was measured.

Similar experiments using UO_2 powder suspensions were also performed. The suspensions contained 0.2 g UO_2 in 20 mL 50 mM HCO_3^- and were purged with N_2O throughout the experiment.

Corresponding reference experiments in unirradiated Ar-saturated solutions were performed and used for background corrections.

Impact of reactive solutes (Paper IV)

The impact of NaCl (2 M), 2-propanol (0.1 M) or Fe(II)(aq) (10 μM) on radiation induced oxidative dissolution of UO_2 was studied in Cs-137 γ-irradiated experiments. A UO_2 pellet was immersed in 10 mL aqueous solution containing 10 mM HCO_3^- or one of the solutes together with 10 mM HCO_3^-. The solution was purged or saturated with one of the following gases; Air, N_2O or inert gas (N_2 or Ar) and the U(VI) concentration in solution was followed as a function of irradiation time.

When Fe(II) was present the solution was buffered with 0.1 M TRIZMA® (Tris(hydroxymethyl)aminomethane) buffer at pH 7.1 and the sample/solution preparation took place in a glove-box with Ar atmosphere containing 0.03 % CO_2 and < 0.1 ppm O_2, in order to avoid precipitation and oxidation of Fe(II) prior to the irradiation.

Reference experiments in N_2 saturated solutions without γ-irradiation under otherwise identical conditions were performed and used for background correction.

The effect of noble metal inclusions (Paper V)

The influence of noble metal inclusions on the UO_2 oxidation by O_2 and solid phase/surface U(VI) reduction by H_2 under Cs-137 γ-irradiation, was studied experimentally using four UO_2 pellets with Pd concentration ranging from 0 to 3 wt.% immersed in 10 mL 10 mM HCO_3^- solution. Oxidation by O_2 was measured in oxygen saturated solution whereas N_2- and H_2-saturated solutions were used in the irradiation experiments. The U(VI) concentration in solution was followed as a function of reaction/irradiation time.

Corresponding reference experiments using N_2-saturated solutions without γ-irradiation were performed and used for background corrections.

Oxidative dissolution of NpO_2 and PuO_2 (Paper VII)

In order to compare the oxidative dissolution behavior of NpO_2 and PuO_2 to that of UO_2, experiments were performed where the reaction between the actinide oxides (depleted uranium, Np-237, Pu-238 and Pu-239) and H_2O_2 were studied by mixing aqueous suspensions of AnO_2 powders with H_2O_2 solutions and monitoring the H_2O_2 concentration and the concentration of dissolved An versus time.

The experiments were performed in gloveboxes except for the experiments measuring H_2O_2 consumption by UO_2 where low O_2 levels were instead ensured by continuous N_2 purging. The oxygen levels in the gloveboxes where in the range of 1 – 2 ppm (NpO_2 and PuO_2) and <0.1 ppm (UO_2).

30 mg actinide oxide powder was mixed with ~20 mM aqueous H_2O_2 solution in a glass vessel. The solution volume was 100 ml in the experiments using NpO_2 and PuO_2 and 20 ml in the case of UO_2. 5 ml samples were taken at several time intervals after the start of the experiment.

At the end of the experiments the oxidation state distribution in the aqueous phase was analyzed. This was done by oxidation state separation by solvent extraction using TTA (thenoyltrifluoroaceton) in the case of Pu and DBM (dibenzoylmethane) in the case of Np according to the method described in reference [77,78], followed by ICP-MS analysis.

Due to the different specific activities of the actinide oxides, the background levels of radiolytically produced H_2O_2 will vary. In order to account for this, background studies were performed for ^{237}Np, ^{239}Pu and ^{238}Pu where the solution consisted of deionised water. Corresponding reference experiments without added H_2O_2 were also performed.

Radiation enhanced reactivity (Paper VIII)

The effect of irradiation of the UO_2 matrix on the kinetics of UO_2 oxidation was studied in four series of experiments. In each series, the same specimen of UO_2 (pellet, fragment or slices) was used throughout in order to avoid deviations caused by differences between different individuals (i.e. differences in geometry).

Permanganate (initial concentration 0.6 mM) in aqueous solutions was used as oxidant in all four series. The reactions were studied as a function of time. In the irradiation experiments, the results were corrected with respect to the radiolytic decomposition of MnO_4^-, measured in separate experiments.

Series 1: In this series several consecutive oxidation experiments (reaction time ~80 min in each experiment) were carried out without irradiation in order to detect possible changes in the reactivity arising from oxidation of the material.

Series 2: In this series the reaction was followed during ~80 minutes Co-60 γ-irradiation of the system.

Series 3: In this series the reaction was followed during electron-irradiation of the system. A custom made PEEK-cell was used, where the solid material (two UO_2 slices) can be placed either inside the cell in contact with the

solution or on the outside in order to provide the same radiation dose but no contact between the solution and the solid. The setup was designed so that nearly all the radiation energy was deposited in the solid and irradiation of the solution was minimized. Irradiation was performed in 1 minute intervals, the total reaction time was ~45 minutes, whereof 15 minutes irradiation. The reactivity was also studied before and after each irradiation experiment.

Series 4: In the last experiment the reaction was studied after electron-irradiation of the solid material in air. The sequence; 2-3 oxidation experiments – irradiation in air – washing with HCO_3^-, was repeated 3 times.

The influence of particle size on the kinetics of UO_2 oxidation in aqueous powder suspensions (Paper IX)

In this study the second order rate constants and activation energies were measured for the reaction between MnO_4^- and UO_2, using suspended UO_2 powder of four different size fractions, < 20 μm, 20 μm – 41 μm, 41 μm – 72 μm and > 72 μm (obtained by sieving). The activation energy for the reaction with a UO_2-pellet was determined in additional experiments. The powders were characterized by measuring the BET surface area and by Scanning Electron Microscopy on fractions 1 (>72 μm) and 4 (< 20 μm).

The powder/pellet was exposed to solutions containing ~0.7 mM MnO_4^- and the oxidant concentration was measured as a function of time. In order to determine the second order rate constant the amount of UO_2 was varied between 20 mg and 40 mg and the solution volume was varied between 20 mL and 100 mL. In the measurement of the activation energy the temperature was varied from 0 °C to 75 °C.

Formation of UO_2 nanoparticles (Paper X)

The synthesis of UO_2 nanoparticles was performed by electron- and γ-irradiation of 10 mM UO_2^{2+} (uranylnitrate) solutions containing 10% 2-propanol, total volume 20 mL. The electron irradiations were performed in 0.5-4 minute intervals. The irradiations were performed in closed glass vessels, and the solutions were purged with Ar prior to the irradiations, in order to prevent oxygen influence.

In the experiments using electron irradiation, the ionic strength and pH were varied (by addition of $NaHCO_3$, Na_2SO_4 and Na_2CO_3) in order to investigate the effects on the particle size distribution and stability of the produced colloidal suspensions. PCS was used to determine the concentration of particles and the particle size distribution of the colloids.

The conversion of U(VI) was determined following the U(VI) concentration in the aqueous phase as a function of irradiation time. In order

to measure the specific surface area (BET) of the particles the solid was precipitated by addition of NaOH. Thereafter, the solution was removed by filtration under Ar pressure and the solid phase was dried in inert atmosphere.

The formation of UO_2 nanoparticles by electron irradiation was also investigated in the absence of 2-propanol. In these experiments, 10 % tert-butanol was used in the reaction solution in order to scavenge $OH^{\bullet}$. The H_2O_2 consumption of these particles was measured.

For the reactivity study, fresh colloidal suspensions were synthesized by electron irradiation (10 mM UO_2^{2+}, 10% 2-propanol in 20 mL solution, as above), total irradiation time 14 min. The produced suspensions were placed in a glove box (inert atmosphere, < 0.1 ppm O_2) directly after irradiation. At the start of each reactivity experiment, the desired amount of UO_2 colloids was withdrawn from the production vessel by pipetting the corresponding suspension volume (assuming that the particles are homogeneously distributed in the solution). Several experiments were performed, with the amount of added colloidal suspension varying from 1.5-3.5 mL (theoretically corresponding to 4.3-10.1 mg of UO_2 powder).

The suspension was added to the reaction solution containing ~0.12 mM H_2O_2 and 10 mM HCO_3^-, total volume 400 mL. The reaction solution was stirred with a magnetic stirrer throughout the experiment. The H_2O_2 concentration in the solution was monitored as a function of time.

Results and Discussion

Oxidation of UO_2 (Paper I-III)

Although the rate of UO_2 oxidation seems to depend solely on the one-electron reduction potential of the oxidant [42], the mechanism for oxidative dissolution follows a more complex pattern. Assuming that the reaction mechanism differs between one- and two electron oxidants according to reaction 16-19 we can expect two electron oxidants to be more efficient than one electron oxidants (per electron pair) in oxidizing U(IV) to U(VI). The main reason for this is that a solid-phase disproportionation process is required for production of the soluble species (reaction 19). Another possibility of forming U(VI) would be if two consecutive one-electron oxidants react at the same site (reaction 17-18), however, at the low oxidant concentrations considered here, the probability for this should be extremely low. Consequently, assuming that U(VI) is the only soluble species, we expect one-electron oxidants to be less efficient (per electron pair) than two-electron oxidants in oxidative dissolution of UO_2.

The oxidative dissolution yield of UO_2 was studied using H_2O_2 (two-electron oxidant) and $IrCl_6^{2-}$ (one-electron oxidant). The results are shown in Fig. 2, were the dissolution yield is plotted versus initial oxidant concentration.

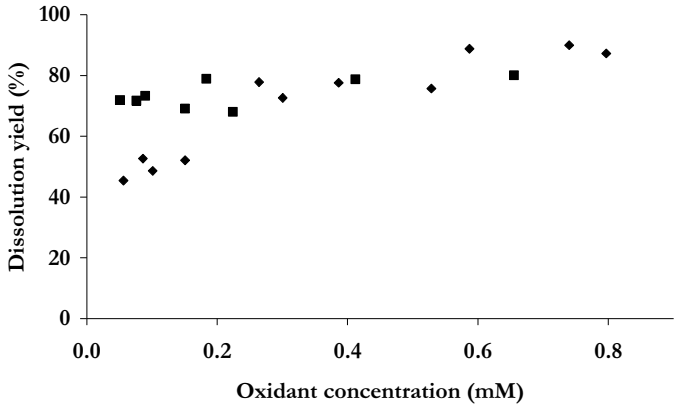

Figure 2. Oxidative dissolution yields for ♦ $IrCl_6^{2-}$ and ■ H_2O_2 plotted versus initial oxidant concentration.

As can be seen in the figure, the dissolution yield (per electron pair) for the one-electron oxidant $IrCl_6^{2-}$ is significantly lower than for the two-electron oxidant H_2O_2 at initial oxidant concentrations below 0.2 mM. The difference in yield supports the theory that U(VI) is the main soluble species and it implies that the disproportionation of surface bound U(V) (reaction 19), is a slow process. This is not surprising given the low electrical conductivity of UO_2(s) [5].

The observed increase in yield with increasing oxidant concentration for the one-electron oxidant $IrCl_6^{2-}$ agrees with the suggested reaction scheme (16-19). At higher initial oxidant concentration the distance between the oxidized sites on the surface decreases which would facilitate the disproportionation process. Furthermore, the probability of two one-electron oxidants reacting at the same UO_2-site (reaction 17-18) increases with increasing oxidant concentration. An interesting observation is that the maximum dissolution yield observed for H_2O_2 is 80% even though the oxidative dissolution is thermodynamically favored. The remaining 20% is probably catalytically decomposed on the UO_2 surface.

Most studies on oxidative dissolution of UO_2 have been conducted using H_2O_2 or O_2 as oxidants. Apart from these oxidants, radiolysis of water also produces a number of oxidizing radical species and their importance for spent nuclear fuel dissolution has been discussed. Judging from the results presented above, we would expect the radicals (one electron oxidants) to be less efficient in dissolving UO_2 compared to H_2O_2 and O_2.

However, from the linear relationship previously determined between the one electron reduction potential and the rate constant for oxidation [42] it can be concluded that $CO_3^{\bullet-}$ and $OH^{\bullet}$ are significantly more reactive towards the UO_2 matrix compared to H_2O_2 and O_2, the former having significantly higher reduction potentials [79,80]. Hence, on the basis of the reactivity alone, the impact of the radical radiolysis products on spent nuclear fuel dissolution can be assumed to be significant although their importance has never been unambiguously proven.

In order to study the relative impact of radical and molecular radiolysis products experiments were performed where the amount of dissolved U(VI) was measured as a function of radiation time in systems dominated by different oxidizing species (obtained by saturating the solution with different gases or gas-mixtures; Ar, N_2O, O_2, air and N_2O/O_2 (80/20 mol%).

Under the conditions used in our experiments, i.e. 10 mM HCO_3^-, oxidation of UO_2 rather than dissolution of oxidized UO_2 has been shown to be the rate limiting step [32]. Hence, the rate of dissolution will be identical to the total rate of oxidation, this in turn being equal to the sum of the rates of

oxidation for all oxidants as described by Eq. 22. This is a prerequisite for comparing the relative impact of the radiolytical oxidants.

$$r_{diss} = \frac{dn_{U(VI)}}{dt} = SA_{UO_2} \sum_{ox=1}^{n} k_{ox}[Ox]\frac{n_{e^-}}{2} \qquad (22)$$

SA_{UO_2} denotes the UO_2 surface area, k_{ox} the rate constant and [*Ox*] the oxidant concentration. n_{e^-} is the number of electrons involved in the redox process (2 for H_2O_2 and O_2 and 1 for the radicals). The measured amount of dissolved U(VI) is shown as a function of absorbed dose in Fig. 3. As can be seen in the figure, the amount of dissolved U(VI) appears to increase linearly with absorbed dose in all cases. Since the absorbed dose is proportional to the irradiation time, the slopes are proportional to the rate of dissolution and thereby to the rate of oxidation.

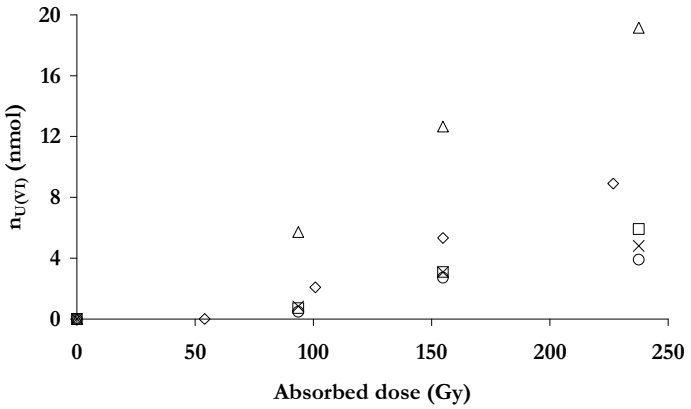

Figure 3. Measured amount of dissolved U(VI) as a function of absorbed dose for different systems; (Δ) O_2, (◊) air, (□) N_2O, (×) Ar, (○) N_2O/O_2.

It is obvious that the dissolution rate is significantly higher for the O_2- and air-saturated solutions where production of $O_2^{\bullet-}$ is enhanced. $CO_3^{\bullet-}$ is produced in all systems, however, there is no significant increase in the rate of dissolution when the G-value is increased by a factor of 2 (N_2O and N_2O/O_2). It should be noted that the oxidizing capability (reflected by the reduction potential) and thereby the reactivity of $O_2^{\bullet-}$ is estimated to be several orders of magnitude lower than that of $CO_3^{\bullet-}$. Hence, the observed

dissolution rates cannot be understood solely in terms of relative reactivity and initial yields of radiolysis products. To further analyze the reaction conditions numerical simulations of water radiolysis in the different systems were performed using MAKSIMA-Chemist* [81], not taking surface reactions into account. From these simulations the concentration of oxidants at different absorbed doses are obtained. Using these data and the rate constant for oxidation of UO_2 by each oxidant and the UO_2 surface area, the theoretical amount of U(VI) can be calculated by numerical integration of Eq. 22.

In the calculations the estimated BET surface area of the pellet was used (the geometrical surface area, 3.66 cm^2, multiplied by three [82]). The U(VI) release as a function of absorbed dose obtained by the calculations are compared to the experimentally determined release rates in Fig. 4.

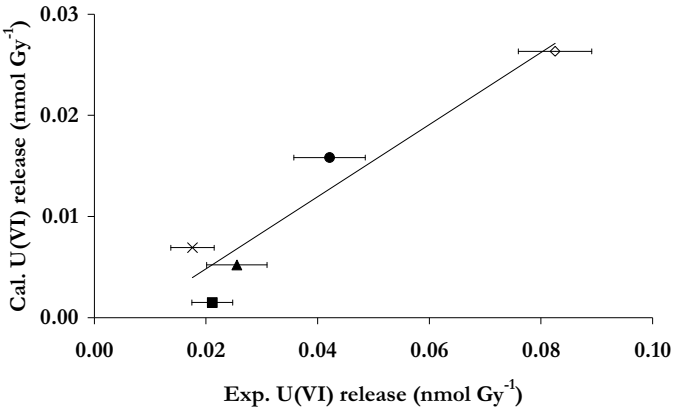

Figure 4. Calculated U(VI) release as a function of absorbed dose plotted versus experimentally determined release for the systems studied; (▲) N_2O, (×) N_2O/O_2 (■) Ar, (●) air, (◊) O_2.

As can be seen the correlation between the calculations and the experimental results are fairly good, at least for the O_2 and air saturated systems where the dissolution rates are relatively high and consequently, the error in experimental determination of the U(VI) concentrations smaller.

Given the correlation between the calculated and the experimentally determined U(VI) release we can use the simulated data to assign the relative

* Reactions and rate constants used are shown in Appendix 1.

impact of the different radiolysis products in the systems studied here. The results are given in Table 3. From the table it is obvious that H_2O_2 has the highest impact on the Ar-, air- and O_2-saturated systems. For the N_2O and N_2O/O_2-saturated systems, $CO_3^{\bullet-}$ has the highest impact. $CO_3^{\bullet-}$ is also of significant importance in the Ar-saturated system. O_2 has significance in all the systems. Not surprisingly, the relative impact of $CO_3^{\bullet-}$ is highest in the two systems where the G-value for $CO_3^{\bullet-}$ is highest.

Table 3. The relative impact of oxidants under γ-irradiation.

	[H_2O_2]	**[O_2]**	**[$O_2^{\bullet-}$]**	**[$HO_2^{\bullet}$]**	**[$CO_3^{\bullet-}$]**	**[$OH^{\bullet}$]**
Ar	72 %	2 %	0 %	2 %	24 %	0 %
N_2O	16 %	4 %	0 %	0 %	79 %	0 %
N_2O/O_2	13 %	24 %	0 %	0 %	62 %	0 %
O_2	70 %	29 %	0 %	1 %	0 %	0 %
Air	90 %	9 %	0 %	3 %	0 %	0 %

The experimental (and simulated) irradiation time is very short in view of spent nuclear fuel dissolution in a geological deep repository. Furthermore, the relative impact of the different oxidants is time dependent. For these reasons we have performed simulations on the γ-irradiated systems for somewhat longer times. These simulations clearly show that at longer irradiation times the relative impact of molecular oxidants increases also in the systems initially dominated by radicals.

In the experiments performed using a UO_2 pellet the UO_2 surface area exposed to the aqueous solution is relatively small and, consequently, the amount of dissolved U(VI) is also relatively small. The experiments are therefore sensitive to uncertainties in the analysis of the U(VI) concentration. We have also studied the amount of dissolved U(VI) as a function of irradiation time using N_2O saturated aqueous UO_2-powder suspensions containing HCO_3^-. In this case the UO_2 surface area exposed to the aqueous solution is significantly larger and the amount of dissolved U(VI) is significantly higher. The experimental results are presented in Fig. 5 along with the corresponding amounts of dissolved U(VI) calculated by the approach described above. As can be seen, the calculated amounts of dissolved U(VI) are very similar to the experimental values. Consequently, the

relatively simple approach used for calculating the rate of UO_2 oxidation/dissolution appears to be very useful.

In general the calculated dissolution rate falls below the experimentally observed dissolution rate. A rationale for this could be the presence of U(VI) in the pellet interior. U(VI) present inside the pellet is not removed by the pre-treatment with HCO_3^-, but becomes accessible for dissolution when the outer UO_2 layers on the pellet surface are oxidative dissolved. In study using a UO_2 pellet, the uncertainty in the estimated surface area is relatively large, leading to relatively large uncertainties in the calculated dissolution rates.

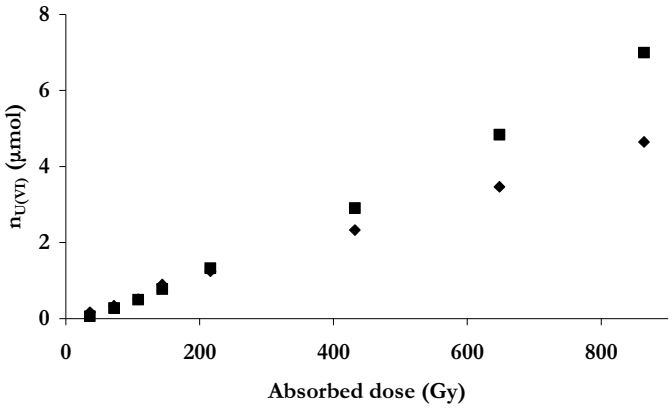

Figure 5. Released amount of U(VI) as a function of absorbed dose in γ-irradiated UO_2 powder suspensions saturated with N_2O; (♦) calculated and (■) experimentally determined.

In a deep repository, the radiation chemistry in the vicinity of the fuel surface will be dominated by α-radiolysis [46]. Therefore, we have performed the same type of simulations on α-irradiated systems using the same dose rate. The results (based on a simulated irradiation time of 6 h) are given in Table 4.

An interesting observation here is that the rate of oxidation is completely dominated by H_2O_2 in all four cases (99.9–100%). $CO_3^{\bullet-}$ is of comparable importance only during the first minute of irradiation. These results show that H_2O_2 is the only oxidant that has to be taken into account when estimating the rate of UO_2 oxidative dissolution under deep repository conditions (granite groundwater dominated by α-radiolysis).

Table 4. Relative impact of oxidants under α-radiolysis.

	H_2O_2	O_2	$O_2^{\bullet-}$	$HO_2^{\bullet}$	$CO_3^{\bullet-}$	$OH^{\bullet}$
No additives	100.0 %	0.01 %	0 %	0.03 %	0 %	0 %
H_2 (40 bar)	99.9 %	0 %	0 %	0.02 %	0 %	0.03 %
H_2 (40 bar) HCO_3^- (10 mM)	100.0 %	0 %	0 %	0 %	0.02 %	0 %
HCO_3^- (10 mM)	99.9 %	0.09 %	0 %	0 %	0 %	0 %

UO_2 dissolution rates (i.e. uranium release) under oxidizing conditions are reported in numerous publications [13]. As mentioned above, these dissolution rates are often specific for the experimental conditions employed and consequently not always applicable to other systems. However, using the previously determined rate constants for the oxidation of UO_2 by different oxidants (see Table 2) and the rate constants for dissolution of UO_2^{2+} from the surface [32] it is possible to compare the various dissolution rates reported in the literature. If the reported rates of dissolution are constant with time, the system can be assumed to be in steady-state. Hence, the rate of dissolution of oxidized UO_2 is equal to the rate of UO_2 oxidation. The steady-state is described by Eq. 23

$$k_{ox}[Ox]SA_{UO_2} = k_{diss}SA_{UO_2^{2+}} \tag{23}$$

where k_{ox} is the rate constant for oxidation of UO_2, $[Ox]$ is the oxidant concentration, SA_{UO_2} is the surface area of UO_2 at steady-state, k_{diss} is the rate constant for dissolution of oxidized UO_2 (= $k_{HCO_3^-}[HCO_3^-]$ in the presence of HCO_3^-) and $SA_{UO_2^{2+}}$ is the surface area of oxidized UO_2 at steady-state. Under these conditions, it is possible to calculate the oxidized fraction of the surface area ($SA_{UO_2^{2+}}/SA_{\text{tot}}$) from the oxidant concentration, the rate constant for oxidation and the rate constant for dissolution of oxidized UO_2 using Eq. 24.

$$\frac{SA_{UO_2^{2+}}}{SA_{UO_2^{2+}} + SA_{UO_2}} = \frac{k_{ox}[Ox]}{k_{diss} + k_{ox}[Ox]} \tag{24}$$

The fraction of oxidized surface area and the rate constant for dissolution (in combination with the HCO_3^- concentration when applicable) can then be used to calculate the rate of dissolution.

As mentioned above, the oxidative dissolution rates reported in the literature are often obtained using H_2O_2 or O_2 as oxidants. The studies considered here were all performed at ambient temperature/25 °C in the presence of H_2O_2 or O_2. Batch and flow experiments as well as electrochemical studies are included.

In the studies found in the literature, oxidation by O_2 was achieved by saturating the solution with air or a gas-mixture with known oxygen content in inert carrier gas. In the case of H_2O_2, the oxidant was added directly to the solution. The pH of the leaching solutions varied from 2.5 to 10, both carbonate-free and carbonate containing leaching solutions were used. In some cases the ionic strength and/or the pH were adjusted by various additives. The UO_2 materials used were powders, with particle size ranging from ~1 μm to ~1 mm, UO_2 discs or pellets.

In Fig. 6, the logarithm of the rate of dissolution determined experimentally in a number of studies [13] is plotted against the corresponding calculated number. The straight line reflects a 1:1 correlation.

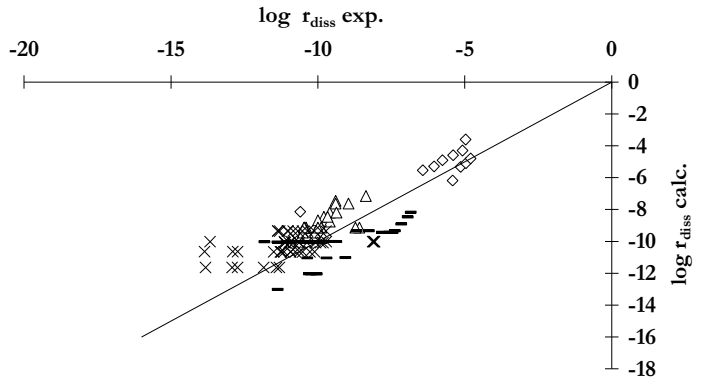

Figure 6. The logarithm of calculated dissolution rates plotted versus the logarithm of experimentally determined dissolution rates [13] for different systems; (◊) H_2O_2 with carbonate, (Δ) H_2O_2 without carbonate, (-) O_2 with carbonate, (×) O_2 without carbonate.

As can be seen, the agreement between the calculated and the experimentally determined dissolution rates is very good for the higher rates while larger deviations are observed for the lower rates. In general, the calculated rates are somewhat higher than the corresponding experimental values. It should be kept in mind that the experimental uncertainties are larger for the lower rates. Furthermore, the calculated rates are partly based on the assumption that the oxidant concentration is constant during the experiment. Any error in the reported oxidant concentration will therefore result in an error (over-estimation) in the calculated dissolution rate.

The effect of reactive solutes and noble metal inclusions (Paper IV-V)

In order to elucidate the effect of potentially reactive solutes present in the groundwater in a future deep repository for spent nuclear fuel, experiments were performed where the effect of NaCl (2 M), 2-propanol (0.1 M) and Fe(II)(aq) (10 μM) on dissolution of UO_2 caused by γ-irradiation was studied under various experimental conditions.

In Fig. 7a the measured uranium release is shown as a function of time for the air-saturated systems. As can be seen in the figure, 100 mM 2-propanol slightly increases the dissolution rate whereas the dissolution rate is significantly decreased in the presence of 2 M chloride.

As can be seen in Table 3 H_2O_2 is by far the most important oxidant when it comes to oxidative dissolution of UO_2 in γ-irradiated, air-saturated systems. Increase in dissolution rate in the presence of 2-propanol can be attributed to a series of reactions leading to increased H_2O_2 production. 2-propanol reacts with $OH^{\bullet}$ (and $H^{\bullet}$) forming a strongly reducing radical (reaction 25). In the presence of O_2, reaction 26 takes place producing $O_2^{\bullet-}$, which proceeds to form H_2O_2 through a number of reactions [18].

$$(CH_3)_2CHOH + OH^{\bullet} \rightarrow (CH_3)_2C^{\bullet}OH \qquad (25)$$
$k = 1.9 \times 10^9$ (L mol^{-1} s^{-1})

$$(CH_3)_2C^{\bullet}OH + O_2 \rightarrow O_2^{\bullet-} \qquad (26)$$
$k = 4.2 \times 10^9$ (L mol^{-1} s^{-1})

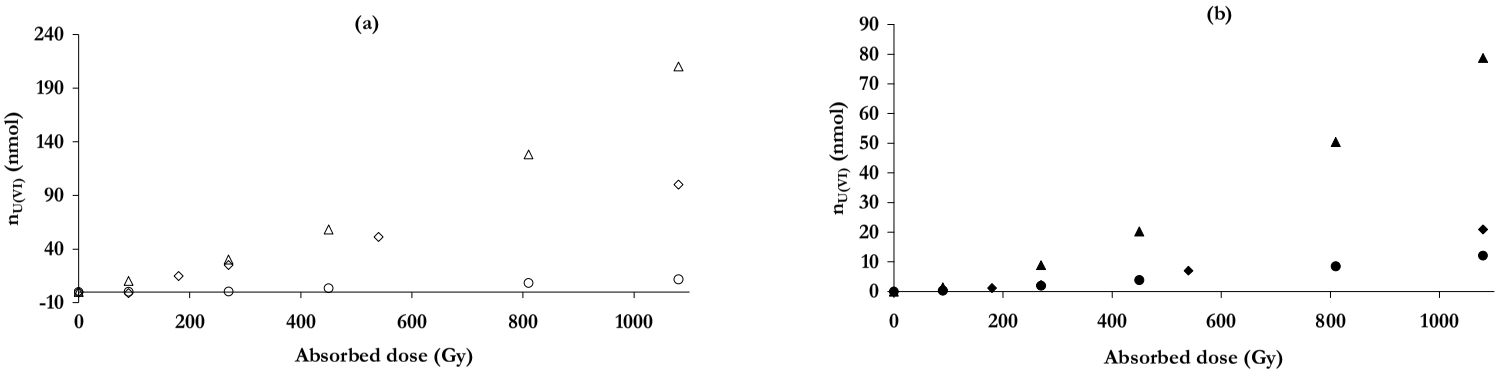

Figure 7. Released amount of U(VI) as a function of absorbed dose for different air-saturated systems (Δ/▲) 2-PrOH (◊/♦) "pure" and (○/●) Chloride. (a) Experimental results, (b) Calculation.

The radical formed by reaction 25 (2-propanol radical) can also scavenge the produced H_2O_2 according to reaction 27 [18].

$$(CH_3)_2C^{\bullet}OH + H_2O_2 \rightarrow CH_3COCH_3 + H_2O + OH^{\bullet} \quad (27)$$
$$k = 7 \times 10^5 (L\ mol^{-1}\ s^{-1})$$

This reaction is however relatively slow compared to reaction 26 and, in this system, the O_2 concentration is significantly higher than the H_2O_2 concentration. Hence, the net effect of 2-propanol addition is an increased H_2O_2 concentration leading to an increased rate of dissolution. Another effect of the 2-propanol radical is reduction of U(VI) back to U(IV), this reaction decreases the amount of U(VI) in solution by approximately 10%. This effect should however, only affect the measured U(VI) concentration in solution and not the rate of UO_2 dissolution.

Judging from the known reactions between Cl^- and the primary products of water radiolysis alone, we would not expect any effect of chloride on the UO_2 dissolution rate. Cl^- reacts with $OH^{\bullet}$ and is eventually converted to $Cl_2^{\bullet-}$ through a series of reactions and when HCO_3^- is present in the system $CO_3^{\bullet-}$ is formed as shown in Appendix 1. At these dose rates radical-radical reactions will be of limited importance and have, for this reason, been excluded from the reaction scheme.

According to the reactions shown in Appendix 1, the final products should be identical to the chloride-free system. However, there are other factors that contribute to the observed decrease in dissolution rate in the chloride system. The most important one is the solubility of oxygen, which deceases with around 50% in 2 M chloride solution [83]. Furthermore, the G-values of the radiolysis products also change with increasing chloride concentrations. In 2 M chloride solution the G-value of H_2O_2 is decreased by nearly 40% [84].

In order to further analyze the systems, MAKSIMA-Chemist [81] was used to perform numerical simulations of radiolysis of the different solutions. In the simulations the reactions discussed above were taken into account as well as the effects on oxygen solubility and G-values.

Using the method described above, the amount of dissolved U(VI) at each sampling point is calculated from Eq. 22. The results are shown in Fig. 7b. As can be seen in the figure, the calculations are qualitatively in good agreement with the experimental results. However, the calculated dissolution rates are generally lower than the experimentally obtained dissolution rates. Looking at the dissolution rates in the systems with added solutes relative to the "pure" air system it can be noted that the impact of chloride is underestimated by the

calculations, whereas the impact of 2-propanol is significantly overestimated. In an experiment performed using 100 mM NaCl solution saturated with O_2 no significant impact of chloride could be measured.

Under the oxygen free conditions (N_2O-system), shown in Fig. 8, both 100 mM 2-propanol and 2 M chloride decreases the UO_2 dissolution rate. In the N_2O-saturated system, $CO_3^{\bullet-}$ (produced from $OH^\bullet$) is responsible for ~80% of the oxidative UO_2 dissolution, whereas H_2O_2 contributes with ~16% (Table 3). When 2-propanol is added $OH^\bullet$ will be effectively scavenged (reaction 25) and the $CO_3^{\bullet-}$ concentration is consequently decreased. The concentrations of oxidants are also affected by the competition between reaction 26 and 27. Since O_2 is in deficit compared to e.g. H_2O_2 the oxidant scavenging reactions e.g. reaction 27 will become increasingly important. The net effect is, practically, extinction of all oxidizing species, which is reflected by the very low dissolution rate.

Calculated U(VI) release, based on numerical simulations using the same method and considerations as described above, are shown in Fig. 8b. As in the air-saturated systems we see a qualitative correlation between the experimental data and the calculations and again the calculated dissolution rates are generally lower than the experimentally obtained dissolution rates. It can also be seen that the impact of chloride is significantly underestimated also in the N_2O-saturated system.

The general overestimation of the amount of dissolved U(VI) can probably be attributed the presence of U(VI) in the pellet interior as discussed above. The release of pre-oxidized uranium from the pellet interior would also explain why negative impact on dissolution rate is underestimated whereas positive impact is overestimated by the calculations.

The fact that, in the N_2O-saturated system, a significant impact of chloride is measured experimentally whereas only a marginal impact is seen in the results from the calculations indicates that not all parameters involved in this system are known. Furthermore, the observed impact of chloride in the N_2O-saturated system is significantly lower than in the air-saturated system. This observation can largely be attributed to the chloride effect on the O_2 solubility in the air-saturated system. This suggests that we cannot fully account for all reactions involving Cl^- and calls for further studies of the chloride system.

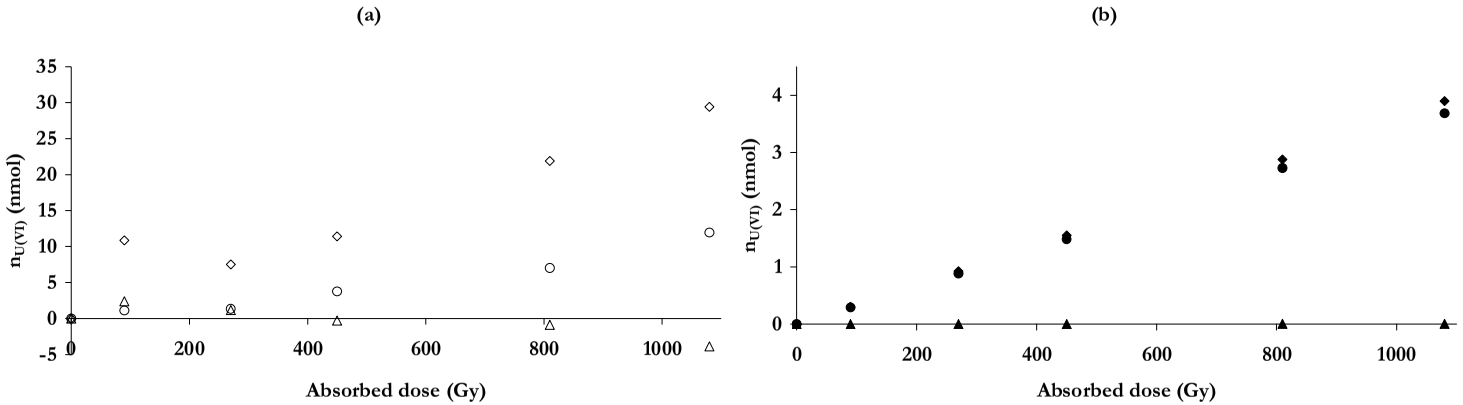

Figure 8. Released amount of U(VI) as a function of absorbed dose for different N_2O-saturated systems; (Δ/▲) 2-PrOH (◊/♦) "pure" and (○/●) Chloride. (a) Experimental results, (b) Calculation.

In Fig. 9 the results from the experiments performed with Fe(II)(aq) are shown together with results from the simulation of the system. As in the previous systems the qualitative agreement is good. The dissolution rate is decreased by the presence of Fe(II)(aq) and (as in the previous systems) the relative impact is somewhat underestimated in the calculations.

In this (Ar-saturated) system both H_2O_2 and $CO_3^{\bullet-}$ will have significant impact on the UO_2 oxidative dissolution (73% and 24% respectively) (Table 3). In presence of Fe(II)(aq) the concentration of both oxidants will be reduced since Fe(II)(aq) is oxidized by both H_2O_2 and $OH^{\bullet}$ (or $CO_3^{\bullet-}$ in HCO_3^- containing solutions) according to reaction 28 (the Fenton reaction) [85] and reaction 29 [18]. Fe(II)(aq) is also capable of consuming other oxidants in the system e.g. $HO_2^{\bullet}$.

$$Fe^{2+} + H_2O_2 \rightarrow Fe^{3+} + OH^{\bullet} + OH^- \quad (28)$$
$k = 6.90 \times 10^4$ (L mol^{-1} s^{-1})

$$Fe^{2+} + OH^{\bullet} \rightarrow Fe^{3+} + OH^- \quad (29)$$
$k = 4.30 \times 10^8$ (L mol^{-1} s^{-1})

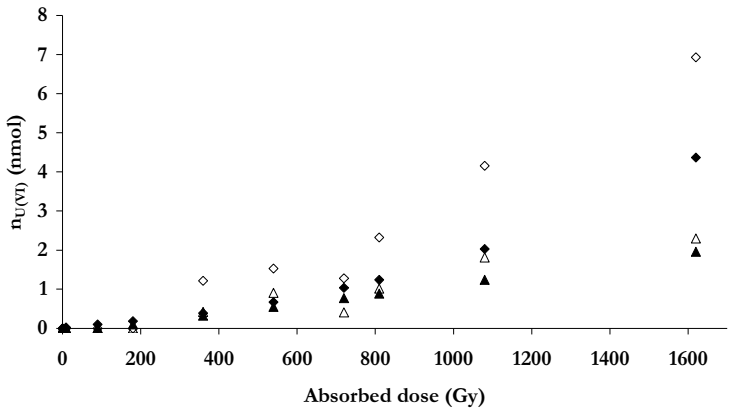

Figure 9. Released amount of U(VI) as a function of absorbed dose for different Ar-saturated systems (Δ/▲) Fe(II)(aq) and (◊/♦) "pure". Filled symbols correspond to calculated U(VI) amounts.

The produced Fe(III) can be reduced back to Fe(II) by e.g. $HO_2^{\bullet}/O_2^{\bullet-}$ or e_{aq}^- causing a self-sustaining cycle regenerating Fe(II). However, at neutral pH the solubility of Fe(III) is low and, with time, Fe(III) will be removed from solution by precipitation.

Fe(II)(aq) is also capable of reducing U(VI) on the UO_2 surface. However, since HCO_3^- is in large excess compared to Fe(II)(aq), the rate of carbonate facilitated dissolution of U(VI) from the surface will be much higher than the reduction even if the reduction is assumed to be diffusion controlled.

As mentioned above, spent nuclear fuel contains nanometer-sized noble metal particles (ε-particles) with catalytic properties. Previous experiments performed using Pd doped UO_2 pellets showed that both the solid phase/surface reduction of U(VI) by H_2 and UO_2 oxidation by H_2O_2 was catalyzed by Pd incorporated in the UO_2 matrix [52].

Using data from reference [52], the catalytic effect on UO_2 oxidation by H_2O_2 can be quantified by plotting the rate of H_2O_2 consumption versus the fraction of palladium. From the slope in this plot the rate constant for the Pd catalyzed oxidation by H_2O_2 was determined to $(1.75\pm0.38) \times 10^{-6}$ m s^{-1}, i.e. more than one order of magnitude higher than the rate constant for the reaction between H_2O_2 and pure UO_2. The diffusion controlled rate constant for this system is calculated to be in the order of 10^{-6} m s^{-1} using Eq. 11. Hence, the Pd catalyzed reaction appears to be diffusion controlled.

It has previously been suggested that also the oxidation of UO_2 by O_2 is catalyzed by ε-particles [7] and electrochemical experiments have shown that the presence of ε-particles leads to a very rapid increases in corrosion potential in the presence of O_2 [49]. This effect is quantified by measuring the dissolution rate of Pd doped UO_2 pellets in O_2 saturated solution. The experiments showed that the U(VI) release rate increases with increasing amount of Pd in the pellet, supporting the suggestion that the reaction between UO_2 and O_2 is catalyzed by Pd.

The rate expressions for the uncatalyzed and catalyzed reactions are shown in Eq. 30 and Eq. 31;

$$r = k_{ox}[O_2] \tag{30}$$

$$r_{cat} = k_{ox}^{Pd}\varepsilon_{rel}[O_2] \tag{31}$$

with k_{ox} and k_{ox}^{Pd} being rate constants for the oxidation of UO_2 by O_2, with and without Pd present as a catalyst, $[O_2]$ the concentration of O_2 and ε_{rel} the fraction of Pd on the pellet surface. The ratio between the U(VI) dissolution

rate in the uncatalyzed case and the total U(VI) dissolution in the catalyzed case is given by Eq. 27;

$$\frac{r}{r + r_{Pd}} = \frac{k_{ox}}{k_{ox} + k_{ox}^{Pd}\varepsilon_{rel}} \tag{32}$$

Eq. 32 can be rearranged in to Eq. 33 expressing the Pd catalyzed rate constant.

$$k_{ox}^{Pd} = \frac{k_{ox}\left[\left(\frac{r_{Pd} + r}{r}\right)\right] - 1}{\varepsilon_{rel}} \tag{33}$$

As the experiments were performed under constant O_2 pressure, the rate constant can be estimated indirectly, based on the experimentally determined U(VI) dissolution rates and the rate constant for the uncatalyzed reaction, using Eq. 28. By this method, the rate constant for the Pd-catalyzed reaction between O_2 and UO_2 is estimated to be in the order of 10^{-7} m s^{-1}.

As the rate constants for the uncatalyzed reactions between UO_2 and the strongest oxidants among the water radiolysis products (e.g. $OH^{\bullet}$, $CO_3^{\bullet -}$) are diffusion controlled [42], Pd/ε-particles can not have any catalytic effect on these reactions.

Experiments performed in non-irradiated systems have shown that the Pd catalyzed reduction of U(VI) by H_2 is approximately diffusion controlled. In order to investigate the effect of H_2 in combination with Pd-inclusions on radiation induced oxidative dissolution of UO_2 experiments were performed where the uranium release from UO_2 pellets with varying Pd-content was measured during γ-irradiation under N_2 and H_2 atmosphere. The results are shown in Fig. 10.

As can be seen in the figure, the uranium release from the pure UO_2 pellet decreases by around 20% in H_2 atmosphere compared to N_2. This can be attributed to reactions between H_2 and the products of water radiolysis, leading to lower concentrations of oxidants and thereby to lower rate of UO_2 oxidation.

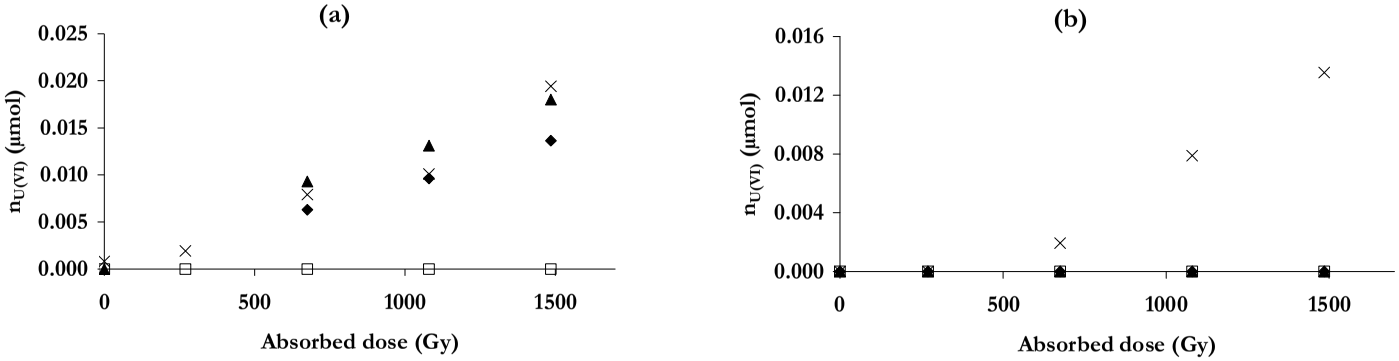

Figure 10. Dissolution of uranyl as a function of absorbed dose for UO_2 pellets containing (×) 0 wt.%, (▲) 0.1 wt.%, (◊)1 wt.%, and (□) 3 wt.% Pd in systems saturated with (a) N_2 and (b) H_2.

Under H_2 atmosphere, the UO_2 dissolution is completely inhibited by the presence of Pd (0.1-3%). Under N_2 atmosphere, 3% Pd is required to inhibit the dissolution. Two process must be taken into account to explain this behavior; (a) the solid phase/surface reduction of U(VI) by H_2 catalyzed by Pd and (b) the Pd-catalyzed oxidation of UO_2 by O_2 and H_2O_2.

The theoretical dissolution rate for pure UO_2 is expressed by Eq. 22, taking the effect of Pd into account Eq. 34 is obtained.

$$r_{diss} = r_{ox} - r_{red} = \sum SA_{UO_2} k_{ox} [Ox] + \sum \varepsilon_{rel} SA_{UO_2} k_{ox}^{Pd} [Ox] - \varepsilon_{rel} SA_{UO_2} k_{red} [H_2] \quad (34)$$

with $r_{diss,}$ r_{ox} and r_{red} being the rates of dissolution, oxidation and reduction respectively, $[Ox]$ the oxidant concentration, k_{ox} and k_{ox}^{Pd} the rate constants for each oxidant, SA_{UO_2} the surface area of the pellet, $[H_2]$ the concentration of H_2 in solution and ε_{rel} the Pd fraction in the pellet.

The theoretical amounts of U(VI) in at the end of each experiment were calculated using the same approach as described above now taking the effect of Pd into account according to Eq. 34. Only oxidation by the molecular oxidants (H_2O_2 and O_2) was assumed to be catalyzed by Pd as discussed above.

The results of the calculations are compared to the experimental values (corrected for background) in Table 5. In some cases, the dissolution in the background experiment exceeds the dissolution during irradiation in the presence of H_2. The net dissolution rates were taken as zero in these cases as the reduction rate can never exceed the oxidation rate on a fully reduced surface. The ratios between the calculated and the measured dissolution rates in cases where dissolution was experimentally observed and calculated are all around 0.1. Again, this can probably be attributed to the presence of U(VI) in the pellet interior. The discrepancy between calculated and experimentally determined dissolution rates is larger here than in the experiments discussed above. The experiments above were performed using commercially produced pellets whereas pellets produced by hot-pressing of UO_2 powder according to the method described in [52] were used in the study of Pd-effects. The latter method probably gives rise to higher levels of pre-oxidized uranium in the pellets. As can be seen in the table, the experimentally observed trends are reproduced by the calculations. The relative impact of the different oxidants on the UO_2 oxidation under N_2 atmosphere is shown in Table 6.

Table 5. Comparison between calculated and experimentally determined U(VI) release.

Cal. U(VI) release μmol Gy^{-1}		**Exp. U(VI) release** μmol Gy^{-1}	
N_2	**H_2**	**N_2**	**H_2**
1.97×10^{-6}	9.80×10^{-7}	$(1.2\pm0.2) \times 10^{-5}$	$(1.1\pm0.2) \times 10^{-5}$
1.25×10^{-6}	0	$(1.4\pm0.2) \times 10^{-5}$	≈ 0
0	0	$(1.0\pm0.2) \times 10^{-5}$	0
0	0	≈ 0	0

Table 6. Relative impact of γ-radiolysis products in N_2 saturated system.

	0 % Pd	**0.1 % Pd**	**1 % Pd**	**3 % Pd**
H_2O_2	98.5 %	41.2 %	6.6 %	2.3 %
H_2O_2 (Pd)	-	56.2 %	90.2 %	94.4 %
H_2O_2 tot	98.5 %	97.4 %	96.8 %	96.7 %
O_2	1.1 %	0.5 %	0.08 %	0.03 %
O_2 (Pd)	-	2.0 %	3.1 %	3.3 %
O_2 tot	1.1 %	2.4 %	3.2 %	3.3 %
$CO_3^{\bullet-}$	0.4 %	0.2 %	0.03 %	0.01 %
$HO_2^{\bullet}$	0.03 %	0.01 %	0 %	0 %

Table 6 reveals that H_2O_2 is the most important oxidant in all studied cases. Naturally, the Pd catalyzed reaction between H_2O_2 and UO_2 becomes increasingly important with increasing amount of Pd on the surface of the pellet. It should however be noted that the total impact of H_2O_2 remains almost constant throughout the series. It can also be seen that O_2 becomes more important with increasing Pd content, due to the catalyzing effect of Pd.

Judging from the results presented here we would expect the rate of UO_2 dissolution under deep repository conditions (i.e. oxygen free) to be significantly decreased by the presence of chloride, Fe(II)(aq) and organic substances capable of forming reducing radicals in the groundwater. Furthermore, reduction of U(VI) by H_2 on the fuel surface catalyzed by noble metal inclusions in the spent fuel is expected to effectively inhibit the radiation induced dissolution of the spent fuel matrix.

Prediction of spent nuclear fuel dissolution rates (Paper VI)

The identification of H_2O_2 as the only oxidant needed to be accounted for when exploring the rate of spent nuclear fuel dissolution significantly simplifies the estimation of the dissolution rate. As mentioned above, using spent fuel inventory data, modeling of the geometrical dose distribution has been performed [46]. On the basis of this, the H_2O_2 production rate as a function of distance from the fuel surface can be calculated. By simulating the H_2O_2 production and consumption by surface reaction, taking diffusion into account, it has been shown that the H_2O_2 surface concentration reaches steady-state within a relatively short time (minutes or hours) compared to the time span of interest with regards to a geological deep repository [86]. Hence, the steady-state approach can be used to calculate the maximum spent fuel dissolution rate. In Fig. 11 the calculated maximum dissolution rate (= H_2O_2 production rate) is shown as a function of fuel age for 38 MWd kgU^{-1} burn up.

The maximum dissolution rate is completely governed by the H_2O_2 production rate and will consequently be unaffected by factors increasing the reactivity of the UO_2 matrix. However, reactions consuming H_2O_2 (other than oxidation of UO_2) will lower the steady-state concentration and thereby the rate of oxidative dissolution will be lowered. In this case the rate constants for the surface reactions and the reactivity of the surface will be of importance, since the competition between surface and bulk reactions will affect the dissolution rate.

The inhibiting effect of Fe(II)(aq) has been proven experimentally as shown above. It was shown that the presence of 10 μM Fe(II)(aq) significantly decreased the UO_2 dissolution rate in γ-irradiated systems. In these experiments the Fe(II)(aq) concentration is likely to decrease with time due to precipitation of Fe(III). In a future deep repository for spent nuclear fuel, the Fe(II)(aq) concentration is not expected to decrease with time. Fe(II) is released from the anaerobic corrosion product (Fe_3O_4) of the canister insert, which can be regarded as a (virtually) infinite pool of Fe(II). Assuming a (steady-state) concentration of Fe(II)(aq) of 1 μM, the dissolution rate is decreased by a factor of 50 as showed in Fig. 11.

Taking the effect of ε-catalyzed reduction of U(VI) by H_2 into account, the dissolution rate can be described by Eq. 34. Assuming ε-particles have the same catalytic ability as Pd, we can calculate the rate of solid-phase reduction using the previously determined rate constant. The results are shown for 1% ε-particle surface coverage in Fig. 11. As can be seen in the figure at this surface coverage, 0.1 bar H_2 would be enough to completely stop the dissolution of 100 year old fuel.

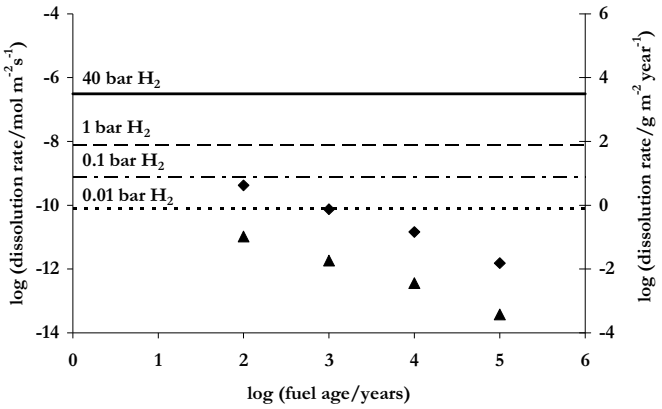

Figure 11. The logarithm of the dissolution rate for spent nuclear fuel (burn up 38 MWd kgU^{-1}) as a function of the logarithm of the fuel age. (♦) maximum dissolution rate. (▲) effect of Fe(II)(aq) (1 μM) consuming H_2O_2 in the bulk. Lines corresponding to the different H_2 partial pressures represent the rates of solid-phase reduction (see Eq. 34).

Oxidative dissolution of NpO_2 and PuO_2 (Paper VII)

In order to elucidate the dissolution behavior of NpO_2 and PuO_2 under oxidizing conditions and compare their behavior to that of UO_2, experiments were performed where the actinide dissolution and oxidant consumption were studied in non-complexing aqueous solutions containing H_2O_2.

In this study, it is, for practical reasons, not possible to determine rate constants. This is partly due to the fact that the solid surface area to solution volume ratio has not been varied and that the conditions are not optimized for pseudo first order kinetics (requires excess of solid reactant). Furthermore, the experiments have been performed utilizing aqueous solutions free from potential complexing agents, such as HCO_3^-. Under these conditions, the kinetics for H_2O_2 consumption is largely limited by dissolution of the oxidized actinide oxide rather than the redox process [32]. For low conversions a steady-state approach can be used. At steady-state, the rate of oxidation is identical to the rate of dissolution as shown in Eq. 23 for UO_2. The rate constants for oxidation by H_2O_2 and dissolution have previously been determined for UO_2 (Table 2) but not for NpO_2 and PuO_2.

Using the present data on H_2O_2 concentration as a function of reaction time, it is possible to determine the relative rates of H_2O_2 induced oxidative dissolution for UO_2, NpO_2 and PuO_2. In Table 7, the initial H_2O_2 consumption rates are shown for the three different actinide oxides.

Table 7. Initial H_2O_2 consumption rates, one-electron reduction potential for the AnO_2^+/AnO_2 redox couple [64] and initial actinide release rates.

	H_2O_2 cons.‡ mol dm^{-3} s^{-1}	**E^0** mV	**An release** mol dm^{-3} s^{-1}
UO_2	4.0	380	9.6×10^{-5}
NpO_2	1.8	640	5.4×10^{-8}
PuO_2	0.36	1040	1.2×10^{-9}

As can be seen, the initial rate of H_2O_2 consumption is highest for UO_2 followed by NpO_2 and the rate for PuO_2 is by far the lowest. When measuring the H_2O_2 consumption, the available surface area of the oxide to solution volume ratio is a critical parameter. The results presented here are based on the assumption that the surface area to volume ratio is equal in the three experiments. Judging from SEM pictures of the materials, the surface area seems to decrease in the order; $PuO_2 > NpO_2 > UO_2$. Since the surface area of the UO_2 powder was estimated to be significantly smaller than for the other materials, the solution volume was decreased by a factor of 5 in those experiments whereas no compensation was made for the difference between NpO_2 and PuO_2. This probably does not compensate fully for the actual differences in surface area, consequently, the trend in oxidant consumption could be even more pronounced than shown here.

Interestingly, the relative trend in reactivity towards H_2O_2 parallels the trend in oxidation potential for the three oxides (as shown in Table 7, UO_2 has the lowest reduction potential while PuO_2 has the highest reduction potential). When using the logarithm of the initial rate of H_2O_2 consumption as a measure of the reactivity and comparing it with the one-electron reduction potential for the AnO_2^+ a linear relationship is found, Fig. 12. Consequently, the consumption of H_2O_2 on these oxides appears to be thermodynamically controlled.

‡ The uncertainty in the initial H_2O_2 consumption rate is approximately 30%.

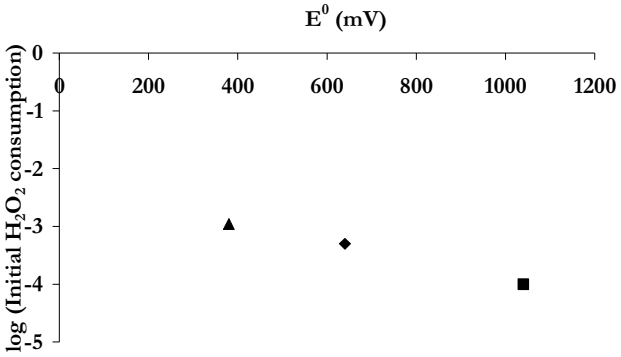

Figure 12. The logarithm of initial H_2O_2 consumption versus the one-electron reduction potential for the AnO_2^+ for (■) Pu, (▲) U and (♦) Np.

It should be kept in mind that the rate of H_2O_2 consumption does not necessarily reflect only the relative rate constant for oxidation of the actinide oxide. The rate constant for dissolution of AnO_2^{2+} will also influence the rate of H_2O_2 consumption in these systems. Thermodynamically, judging from the relative acidity of the actinyl ions, the solvation energy appears to increase in the order $PuO_2^{2+} < NpO_2^{2+} < UO_2^{2+}$. Assuming linear free energy relationships are applicable, the rate constant for dissolution of AnO_2^{2+} should follow the same trend. It is also reasonable to assume that the rate constant for oxidation of AnO_2 by H_2O_2 increases with decreasing potential of the actinide oxide, i.e. in the order $PuO_2 < NpO_2 < UO_2$. Both these effects act in the same direction as the experimentally observed trend, however, it is impossible to assess the relative importance of the two effects on the basis of current data. The observed trend is qualitatively confirmed by the initial rate of actinide release (Table 7).

In the initial phase of the experiments the actinide concentration increases with increasing reaction time in all three cases. At longer reaction times the concentration of U and Np decreases, whereas the Pu concentration continues to increase. This can probably be attributed to the larger propensity of U and Np to form solid peroxide complexes (as mentioned earlier the Pu peroxide complexes are less stable at room temperature). When analyzing the distribution of oxidation states in the dissolved Np and Pu at the end of the experiments performed in the presence of H_2O_2 and in the background experiments, it was found that H_2O_2 addition increased the fraction of

oxidized material (Table 8). This indicates that an oxidation reaction is indeed involved in the dissolution mechanism. It should also be noted that, while the redox reactivity of the actinide oxides towards H_2O_2 is expected to depend on the redox potential of the actinide oxide, the rate of surface catalyzed decomposition of H_2O_2 is expected to be independent of the redox properties and therefore similar for all three oxides. As mentioned above, this has previously been observed for other metal oxides. As a direct consequence, the oxidative dissolution yield is expected to decrease in the order UO_2 > NpO_2 > PuO_2.

Table 8. Fraction of oxidized (oxidation state V and VI) actinide in solution at the end of the experiment.

	Background experiment	**Experiment with added H_2O_2**
NpO_2	0.41	0.93
PuO_2	0.78	1.03

Based on the dissolution rates obtained here, we would not expect the dissolution of the actinides to be congruent. Instead, in a system without complexing agent, the rates of Np and Pu release are expected to be lower than the U release rate. However, in the presence of complexing agents and in systems where the oxides occur in mixed phases these dissolution rates may not be applicable.

Studies of mixed $(U,Th)O_2$ have shown that the normalized Th dissolution rate appears to be unaffected by the presence of uranium. The normalized rate of U-dissolution, on the other hand, is significantly lower for the mixed oxide compared to pure UO_2 and the effect seems to increase with increasing Th-fraction. This indicates that the dissolution behavior of mixed oxides is complicated and cannot be directly predicted from the dissolution rates of the pure phases.

Effect of irradiation on the reactivity of UO_2(s)(Paper VIII)

Due to its content of radionuclides, the spent fuel is continuously being exposed to self-irradiation. As mentioned above, the energy deposition in the material could influence its reactivity. The effect of irradiation on UO_2 reactivity was investigated in four experimental series (series 1-4 as denoted in experimental details), where the reaction between MnO_4^- and UO_2 (irradiated and not irradiated) was studied.

Since the same specimen of UO_2 was used throughout each series the possible effects of repeated oxidation of the surface needed to be investigated. Hence, eight consecutive experiments where a UO_2 specimen was exposed to MnO_4^- solution in the absence of a radiation field were performed (series 1). No difference in reactivity was observed between these experiments. Thereafter, the reaction was studied during irradiation using a Co-60 γ-source (series 2). In these experiments no changes in reactivity arising from the irradiation could be detected. The dose rate applied to the material was then increased in two experimental series performed using an electron accelerator. In series 3 the irradiation were performed using an electron accelerator at three different pulse frequencies 12.5, 25 and 50 Hz corresponding to three different average dose rates; 24.3, 48.6 and 97.2 Gy s^{-1}, respectively (assuming the dose rate to be proportional to the pulse frequency).

These experiments revealed a significant increase in reactivity during the first irradiation (at 12.5 Hz) compared to the unirradiated UO_2. At this dose rate the reactivity after irradiation was identical to the reactivity during irradiation in contrast to the higher dose rates, where the reactivity of the material was higher after the irradiation compared to during irradiation. This indicates that at the beginning of irradiation a relatively low dose gives an instant effect on the reactivity whereas the effect thereafter seems to be delayed.

Assuming that the increase in reactivity caused by one irradiation experiment is maintained in the proceeding experiment (i.e. reactivity after irradiation experiment $n \leq$ reactivity during irradiation experiment $n+1$) we can compare the reactivity of the unirradiated material to the reactivity of the material exposed to a certain dose.

In Fig. 13 the change in UO_2 reactivity (expressed by the change in MnO_4^- consumption) is plotted as a function of total accumulated dose (including γ-experiments).

As can be seen in the figure a threshold dose must be reached before the reactivity effect appears. Judging from the γ-experiments the threshold is above 200-300 Gy. Above the threshold the reactivity seems to increase linearly with absorbed dose. A dose of ~150 kGy increased the reactivity ~2.5 times.

In the fourth series of experiments a fragment of UO_2 was irradiated in air (3 times of 15 minutes each) in the electron accelerator at 50 Hz and the reactivity was studied before and after irradiation. The results are shown in Fig. 14.

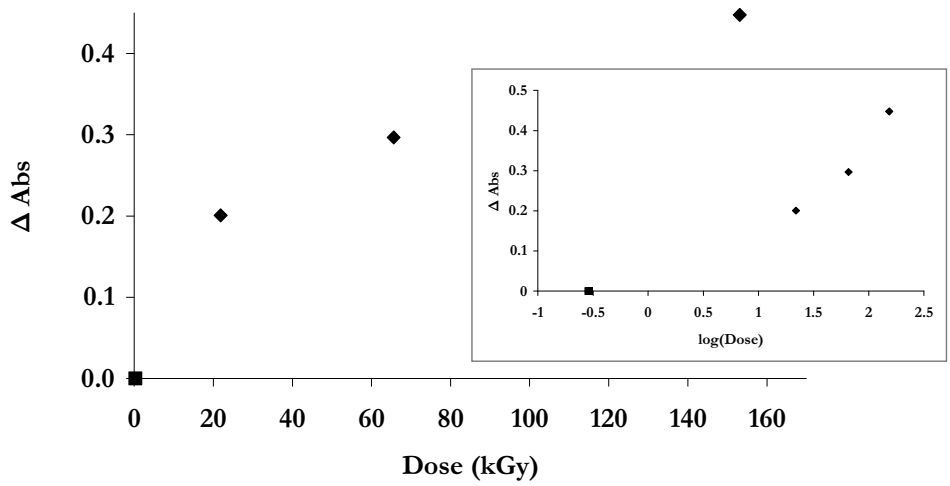

Figure 13. Change in UO_2 reactivity (expressed by the change in MnO_4^- consumption) as a function of total accumulated dose; (■) γ-irradiation (♦) electron irradiation. Insert: Change in UO_2 reactivity as a function of the logarithm of the accumulated dose.

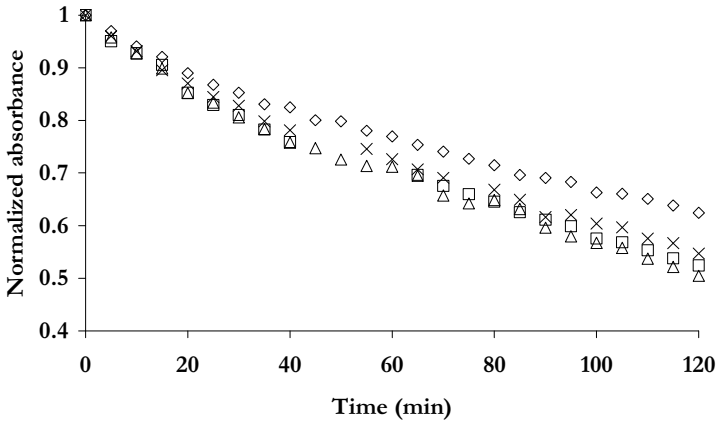

Figure 14. Normalized MnO_4^- absorbance plotted versus reaction time for reaction with UO_2 before and after irradiation in air. (◊) before irradiation, (×) after one irradiation (87 kGy), (Δ) after two irradiations (174 kGy), (□) after three irradiations (262 kGy)).

From these experiments it is clear that the UO_2 reactivity increases upon irradiation. As in the previous series the effect is most pronounced at the beginning of irradiation. Here the effect seems to be limited to about 1.3 times the reactivity before irradiation (based on the consumed amount of permanganate at the end of the experiments). Even though the total dose in these experiments is significantly higher compared to the wet irradiation experiments, the observed increase in reactivity is approximately 50% lower.

Effect of particle size on the kinetics of UO_2 oxidation (Paper IX)

Because of its usefulness as model system for spent nuclear fuel, UO_2 powder is commonly used in kinetic studies of the oxidative dissolution of UO_2. In order to relate different studies made on powder suspensions to each other and to the spent nuclear fuel system, it is of importance to elucidate the particle size dependence of the kinetic parameters for UO_2.

Judging from Eq. 11 we would expect the rate constants to be inversely proportional to the particle size, provided that the activation energy is constant. The second order rate constants determined for the reaction between UO_2 and MnO_4^-, using four different size fractions of UO_2 powder (Table 9) seem to follow this trend quite well.

Table 9. Experimentally determined second order rate constants for the reaction between UO_2 and MnO_4^- four size fractions of UO_2 powder.

Fraction	Particle radius (μm)	k (m s^{-1})
1 (>72 μm)	40	$(10 \pm 1) \times 10^{-7}$
2 (41-72 μm)	28.5	$(8 \pm 3) \times 10^{-7}$
3 (20-41μm)	15.5	$(3.2 \pm 0.5) \times 10^{-6}$
4 (<20 μm)	7	$(6 \pm 1) \times 10^{-6}$

Furthermore, the experimentally determined activation energies for the reaction also show a significant dependence on particle size. The relative activation energies are calculated using fraction 2 (41-72 μm) as reference, this fraction will be used as reference throughout. In Fig. 15 the experimentally determined activation energy is plotted as a function of particle size together with activation energies calculated from Eq. 13, as can be seen from the figure the agreement is satisfactory. The error bars correspond to the uncertainty in each of the experimentally determined activation energies.

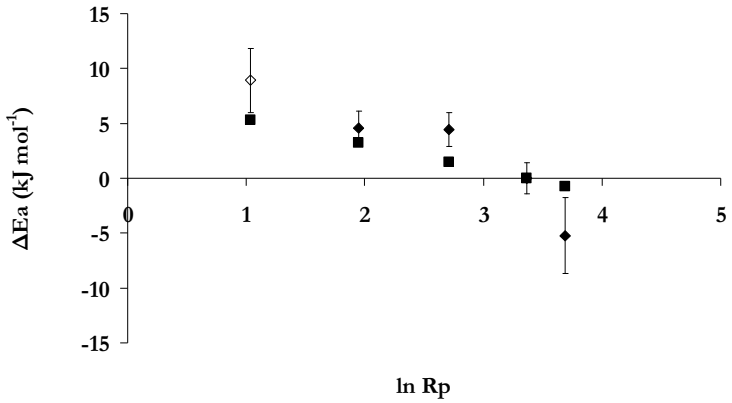

Figure 15. Experimental (♦/◊) and theoretical (■) relative activation energies for the reaction between UO_2 and MnO_4^- plotted versus ln R_p for four size fractions of (♦) UO_2 powder and (◊) a UO_2-pellet.

As shown above, when taking the particle size dependence of the activation energy into account, no effect on the rate constant from a change in particle size is expected. This is not consistent with the experimentally determined second order rate constants presented in Table 9. These rate constants where however obtained based on the measured BET surface area of the powder fractions. If we instead use the geometrical surface area when calculating the rate constants the correspondence with theory is better as shown by the relative rate constants presented in Table 10 and Fig. 16. This indicates that the BET surface area is not an accurate measure of the surface area accessible to the oxidant.

Table 10. Experimentally determined relative second order rate constants for the reaction between UO_2 and MnO_4^- for four size fractions of UO_2 powder based on BET surface area and geometrical surface area respectively.

Size fraction	k_{rel} (BET-surface area)	k_{rel} (geom. surface area)
1 (>72 μm)	1.3	1.8
2 (41-72 μm)	1.0	1.0
3 (20-41μm)	4.2	2.3
4 (<20 μm)	7.9	2.0

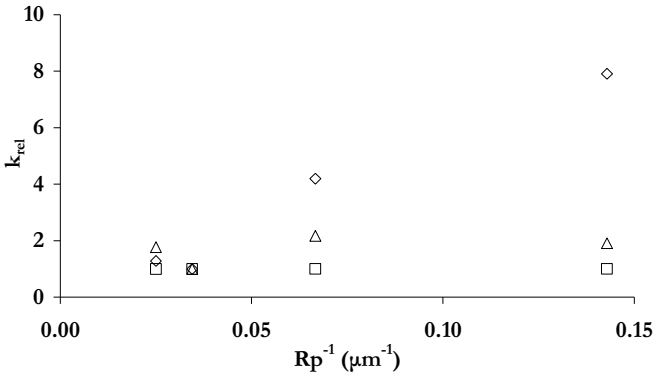

Figure 16. Relative second order rate constants for the reaction between UO_2 and MnO_4^- plotted versus R_p^{-1} for four size fractions of UO_2 powder. Experimental rate constants, based on BET surface area (◊) and geometrical surface area (Δ), respectively, compared with theoretical rate constants (□).

The activation energy for the reaction was determined to 22.2 kJ mol^{-1} when a UO_2-pellet was used as solid phase. If we regard the pellet as one large particle ($R_p \approx 0.5$ cm) we would expect the activation energy of the pellet to be ~2.5 kJ mol^{-1} based on Eq. 13 and results from the powder experiments. However, in view of the pellet composition, i.e. that the pellet consists of pressed and sintered UO_2 powder, the pellet could be considered as a cluster of smaller particles and the experimentally determined activation energy is then not that surprising. In Fig. 15 we have included the relative measured activation energies the pellet (using the grain size of the pellet, $R_p = 2.82$ μm, as reported by the supplier).

As can be seen from the figure the agreement between the powder experiment and the pellet experiment, when treating the pellet as a cluster of small particles, is very good as well as the agreement with theory, considering the uncertainty in the experimental data. A decrease in particle size (to a grain size of 1 to 2 μm in diameter) on the surface of the fuel pellets compared to the fresh fuel has been observed in high burn-up spent nuclear fuel [57]. Consequently, we would expect the activation energy to be even higher for the spent fuel than measured for the UO_2-pellet. If the grain size for example should decrease to 1 μm diameter, the activation energy would increase to 23.4 kJ mol^{-1}. The pre-exponential factor (collision frequency) is however, not affected by a change in grain size as it is governed by the pellet size.

Using the linear relationship between the reduction potential and the second order rate constant established by Ekeroth and Jonsson [42], the activation energies can be calculated for UO_2 oxidation by other oxidants as well. For H_2O_2 and O_2 (E^0=0.46 and -0.15 V respectively [79]) the activation energy was calculated to 24.5 kJ mol^{-1} and 36.8 kJ mol^{-1}, respectively for reaction with a fuel pellet of grain size 5.64 μm.

Formation and reactivity of UO_2 nanoparticles (Paper X)

In reducing parts of a geological deep repository for spent nuclear fuel, U(VI) dissolved from the fuel surface can be reduced to U(IV), which might coalesce and form nanometer-sized UO_2 particles. From the results presented above we would not expect the particle size to have any impact on the reactivity of UO_2. The particles considered above were however, all of micrometer size and that smaller particles (nanometer range) could behave differently from bulk material due to quantum mechanical effects as discussed above.

Radiation chemical synthesis is a well known method for production of nanoparticles of semiconductors [87-89] and metal oxides, and the conversion of U(VI) to U(IV) by reducing radiolysis products in organic solvents has been studied to some extent by Dzięgielewski *et. al.* [90-93]. Here we have used this method (employing γ- and electron irradiation) to produce UO_2 nanoparticles. Furthermore, the reactivity of the produced particles towards H_2O_2 is investigated.

PCS measurements of the colloids produced by electron irradiation at pH=3 and I=0.03 M revealed a narrow size distribution around 22-35 nm and the measured BET surface area after precipitation was 60-70 $m^2 g^{-1}$.

The colloidal suspensions produced at high ionic strength (I=0.18 M), on the other hand, were not stable and the measured initial particle size was significantly higher, around 400 nm. The rationale for this is that increasing ionic strength decreases the repulsion between colloidal particles and thus facilitates aggregation. When varying the pH (3.6, 5.45, 7 and 11.4) at constant ionic strength (I=0.18), it was found that the smallest particles (and the highest number of particles) were formed at pH=11.4. This indicates that the stability of the colloid suspension increases with increasing pH. This is reasonable since pH=11.4 is far from the pzc* and the particles are highly charged (high surface potential), which increases the repulsion between colloidal particles, thus preventing aggregation. The aggregation/precipitation (studied at pH 5.45 and 11.4) seems to follow first order kinetics.

* The point of zero charge (pzc) of UO_2 has been determined to pH=5-5.5 for I=0.1 and I=0.01 M [95].

The conversion of uranyl (at I=0.03 and pH=3), determined from the measurement of U(VI) in solution after irradiation, is shown as a function of absorbed dose and irradiation time in Fig. 17. As can be seen, the conversion increases linearly with absorbed dose up to ~85%, after which the conversion rate decreases. The maximum conversion (95%) is reached at about 15 kGy. The radiation chemical yield (G-value) of reducing radicals in this system is 0.56 μmol J^{-1}. Since each reducing radical transfers only one electron, the theoretical yield of U(IV) is 0.28 μmol J^{-1}. Based on U(VI) consumption in our experiments, assuming reduction to be the only process responsible for removal of U(VI) from solution, the calculated yield of UO_2 is ~1.4 μmol J^{-1}. This is higher than the theoretical yield, indicating that the produced solid also contains uranium of higher oxidation states, as observed earlier by Dzięgielewski *et. al* [92]. Based on the calculated yield, only ~20% of the total uranium content in the powder consists of U(IV). Apart from U(IV), U(V) and U(VI) are probably also present in the produced solid, either co-precipitated with U(IV) or sorbed to the surface of the nanoparticles.

The conversion of uranyl in the tert-butanol system is shown in Fig. 17. In these systems the solvated electron (G-value 0.28 μmol J^{-1}) is the only reducing radical present and the G-value calculated based on uranyl conversion is 0.8 μmol J^{-1}. This is in good agreement with the observations in the 2-propanol system and indicates that the powder produced in the tert-butanol system also consists of ~20% U(IV).

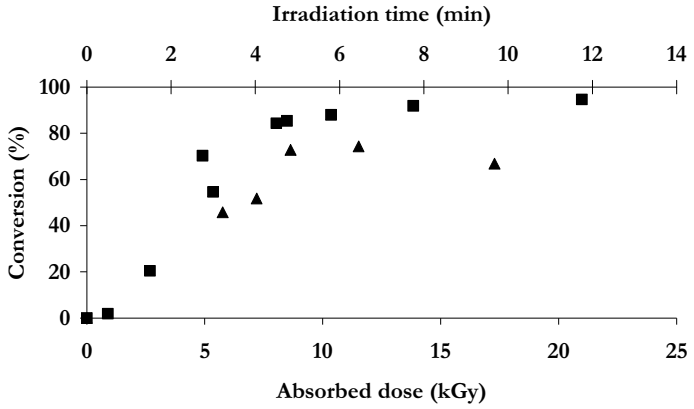

Figure 17. Conversion of U(VI) as a function of irradiation time and absorbed dose, electron irradiation (■) 2-PrOH system, (▲) t-BuOH system.

Production of nanoparticles in the Co-60 γ-source required considerably longer irradiation times compared to electron irradiation, due to the low dose rate. The particle size increased with irradiation time and after ~7 days of irradiation it was around 80 nm, i.e. significantly larger than the particles produced by electron irradiation. This is consistent with the relationship between dose rate and size of the produced particles discussed in reference [94].

The conversion of uranyl (at pH=3 and I=0.03) is shown as a function of irradiation time and dose in Fig. 18. The initial production rate gives a G-value of ~0.3 μmol J^{-1} which agrees quite well with the theoretical yield (0.28 μmol J^{-1}). As can be seen in the figure the production rate is reduced and the system seems to reach steady-state after about 70 hours of irradiation. The maximum conversion reached is ~65%.

The maximum conversion is significantly lower compared to the electron irradiated system. This could perhaps be attributed to the production of H_2O_2 during irradiation. In the γ-irradiated case, a higher dose is required to reach the maximum conversion, leading to a higher amount of H_2O_2 being produced in the system. It is possible that the limit of 65% conversion is due to a steady-state between UO_2 nanoparticle production and consumption by radiolytically produced H_2O_2.

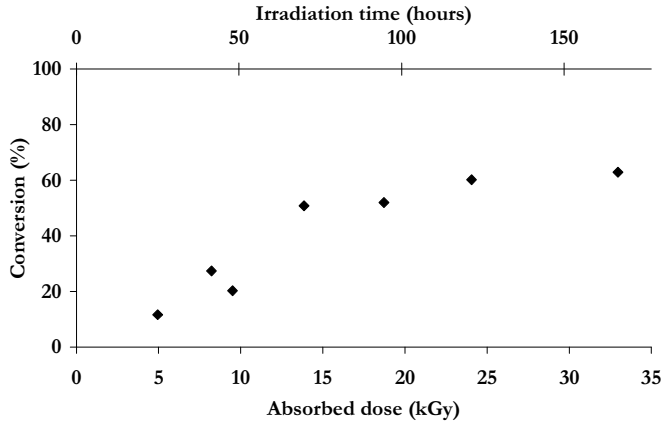

Figure 18. Conversion of U(VI) as a function of irradiation time and absorbed dose, γ-irradiation.

When studying the reactivity in this kind of system, the goal is normally to determine the second order rate constant. The procedure for this has been described above. A prerequisite for this type of experiments is that the reaction rate gives reasonable sampling times. Usually, this can be achieved by an appropriate choice of the amount of solid material and the solution volume (i.e. the surface area/volume ratio). Furthermore, the initial oxidant concentration must be low enough to maintain the excess of solid material, but high enough to obtain measurable changes in concentration as the reaction proceeds. In the present system, the large specific surface area of the UO_2 particles made this impossible. Only an unreasonably large reaction volume, which would have influenced the mixing of the system, would have given a measurable first order reaction rate. Consequently, we can not determine the second order rate constant, but we can nevertheless estimate the rate constant, using the initial rate of H_2O_2 consumption.

In Fig. 19 the normalized H_2O_2 concentration is plotted versus reaction time. As can be seen in the figure, H_2O_2 is in excess in all the experiments, i.e. is not completely consumed at the end of the experiment (when all UO_2 is consumed).

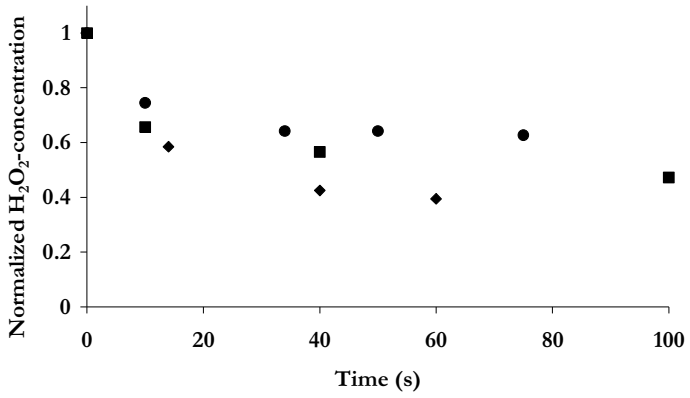

Figure 19. Normalized concentration of H_2O_2 as a function of reaction time, for different amounts of added UO_2 powder; (●) 4.3 mg, (■) 7.2 mg, (♦) 10.1 mg.

As presented above, results from experiments performed on micrometer-sized (~8 μm) UO_2 particles show that approximately 80% of the total amount of consumed H_2O_2 leads to oxidation of UO_2. This could however change when reducing the particle size to nanometer-scale. The magnitude of the catalytically decomposed H_2O_2 fraction is given by the ratio between the rate constants of the two competing reactions (oxidation of UO_2 and catalytic decomposition). The pre-exponential factor should be equal for the two reactions regardless of the particle size (assuming similar surface structure), since it is determined by the rate of diffusion in the system. If the particle size effect on the activation energy follows Eq. 13, the difference in activation energy between the two reactions should also remain constant when going from bulk material to nanoparticles. However, Eq. 13 was only derived for redox reactions and there are indications that the activation energy for catalytic decomposition is insensitive to changes in particle size and the type of metal oxide [96]. In this case, assuming that Eq. 13 is valid for the oxidation of UO_2, the activation energy for oxidation of the nanometer-sized (~30 nm) material is calculated to be 10.6 kJ mol^{-1} higher than the activation energy for the catalytic decomposition.

The difference in activation energy can also be estimated based on the measured G-value for uranyl and the measured H_2O_2 consumption. From this data the catalytically decomposed H_2O_2 fraction is estimated to ~80%, corresponding to a difference in activation energy of around 7 kJ mol^{-1}. Considering the fairly large uncertainties this agrees relatively well with the activation energy difference calculated above.

The initial reaction rate for the nanometer-sized UO_2 is obtained from the initial slope in Fig. 3. By dividing the initial reaction rate by the initial H_2O_2 concentration and UO_2 surface area to solution volume ratio, a minimum value of the second order rate constant can be estimated. The estimated rate constant is $\sim(2.5\pm1) \times 10^{-5}$ m s^{-1}, i.e. significantly higher than for the micrometer-sized powder (Table 2).

Mennecart *et. al.* and Grambow *et. al.* have studied the dissolution and corrosion behavior of α-irradiated [97,10] and α-doped [98] UO_2 colloids of 3 nm size. The α-irradiated experiments indicated that the dissolution/ corrosion behavior of the nanoparticles was similar to that of bulk UO_2. For the α-doped material the results were more difficult to interpret, but the authors claim that their results are in the range of previous results obtained for UO_2 pellets [99] and discs [100]. It should however be stressed, that the dissolution rate is not identical to the rate of oxidation unless steady-state is reached. Studies of the effect of HCO_3^- on the kinetics of UO_2 oxidation by H_2O_2 have shown that below 1 mM HCO_3^- both the oxidation and the dissolution governs the reaction, whereas for higher HCO_3^- concentrations

the reaction is completely governed by oxidation [32]. Since the studies of UO_2 colloids by Mennecart *et. al.* [97,98] and Grambow *et. al.* [10] were all performed in the absence of HCO_3^-, the true rate constant for oxidation can not be extracted from these data and consequently, not compared to the results of the present work.

According to the relationship between the particle size and the activation energy given by Eq. 13, a decrease in particle size from 8 μm to 30 nm would lead to an increase in activation energy by 14 kJ mol^{-1} and, according to Eq. 11, the pre-exponential factor would increase by a factor of 267. As mentioned earlier, theoretically these effects are expected to cancel each other, and no change in the rate constant is expected.

The theoretical increase in pre-exponential factor is very close to the experimentally observed increase in rate constant (~250). This indicates that there is no significant particle size effect on the activation energy, this might seem is surprising considering the expected quantum mechanical effects discussed in the introduction and the results from the experiments using micrometer-sized powder presented above.

However, since a large fraction of the H_2O_2 is catalytically decomposed (~80%) and the activation energy for this reaction is expected to be independent of particle size, the particle size dependence of the oxidation reaction will probably be of minor importance for the overall reactivity. In addition, due to the different methods of powder production, the surface structure of the materials (micrometer- and nanometer-sized powders) are not expected to be identical and consequently, the rate constants obtained for the two powder types are not directly comparable. Furthermore, the relationship between the particle size and the reaction rate (Eq. 11) is only valid for perfectly spherical particles. Since we do not have the possibility to synthesize completely spherical and monodisperse particles, it is impossible to accurately quantify the particle size effect on the pre-exponential factor in a real system.

Conclusions

From this work we can conclude that one electron oxidants are less efficient than two electron oxidants in oxidative dissolution of UO_2 at low oxidant concentrations. This supports the reaction mechanisms suggested for the different oxidant types. It has been shown, on kinetic grounds, that H_2O_2 is the only oxidant needed to be accounted for in radiation induced oxidative dissolution of UO_2 under deep repository conditions (granite groundwater dominated by α-radiolysis). Furthermore, previously determined rate constants for UO_2 oxidation and dissolution of U(VI) from the surface are successfully used to reproduce numerous UO_2 dissolution rates reported in the literature. Consequently the reported rate constants are internally consistent and the proposed mechanism is a sufficient description of oxidative dissolution of UO_2 under various conditions.

By using oxidant concentrations obtained by numerical simulation of radiolysis in homogeneous systems and rate constants for UO_2 oxidation, U(VI) release rates in γ-irradiated systems under different experimental conditions have been reproduced. These studies show that chloride, Fe(II)(aq) and organic substances capable of producing reducing radicals significantly lower the rate of radiation induced oxidative dissolution of UO_2 under oxygen free conditions. The impact of Fe(II)(aq) and organic substances is explained by reactions between the solutes and water radiolysis products leading to decreased oxidant concentrations. The effect of chloride is to some extent rationalized by changes in oxygen solubility and G-values in the system. Interaction with radiolysis products is probably important also in this system but this remains to be proven. It has also been shown that noble metal (Pd) inclusions in the UO_2 matrix effectively inhibit radiation induced dissolution of UO_2 when H_2 is present. This effect is attributed to the solid phase/surface reduction of U(VI) by H_2 catalyzed by Pd.

In a future deep repository for spent nuclear fuel the latter process is expected to effectively inhibit dissolution of the UO_2 matrix. The presence of chloride, Fe(II)(aq) and organic substances capable of producing reducing radicals in the groundwater surrounding the spent fuel act in the same direction by scavenging of oxidants. In a future deep repository, UO_2 nanoparticles can be produced by radiation chemical reduction of U(VI) released from the spent fuel. Such particles are highly reactive towards H_2O_2 and may also contribute to the scavenging of oxidants.

The identification of H_2O_2 as the only oxidant of importance in radiation induced dissolution of spent nuclear fuel significantly facilitates the prediction

of spent fuel dissolution rates. The maximum dissolution rate is equal to the H_2O_2 production rate and consequently, independent of the UO_2 reactivity. More realistic dissolution rates can be obtained by considering the effects of reactive solutes. In order to account for these effects the reactivity of the spent fuel matrix has to be known since the spent fuel dissolution rate, in this case, is affected by the competition between bulk and surface reactions.

The reactivity of the spent fuel matrix is not expected to be identical to the reactivity of pure UO_2. In this work it has been shown that noble metal inclusions in the UO_2 matrix catalyze the oxidation of UO_2 by H_2O_2 and O_2. Furthermore, energy deposition in the UO_2 matrix (by irradiation) also increases the matrix reactivity.

Theoretically, no influence of particle size on the reactivity (rate constant for oxidation) is expected. The results in this work suggest that for a UO_2 pellet, the particle size dependence of the pre-exponential factor is governed by the pellet diameter whereas the particle size dependence of the activation energy is governed by the grain size. Since the pellet diameter is expected to be unchanged during the use of the fuel in the reactor, whereas the grain size in general decreases, this would lead to decreased reactivity of the material. This effect is however counteracted by the increased surface area caused by the decreased grain size as well as by cracking of the fuel.

Results presented in this work show that the rate of NpO_2 and PuO_2 dissolution in a H_2O_2-containing system without complexing agent are lower than the UO_2 dissolution rate. It is however not clear how these actinide oxides behave in the presence of complexing agents or how/if the dissolution rates of the pure oxides can be related to mixed oxides.

To summarize, the mechanisms and kinetics for oxidative and radiation induced dissolution of UO_2, as well as radiation chemistry of dilute aqueous solutions (solute concentrations in the mM-range or lower), can now be considered as well known. Future studies should be focused on elucidating factors influencing the reactivity of the solid fuel matrix. Such factors are, for example, fuel cracking, doping, (self)-radiation, grain size and inhomogeneities in the fuel composition.

Acknowledgements

First of all, I would like to thank my supervisor Professor Mats Jonsson for great support and guidance during the past years. It has been a pleasure working with you.

I would also like to express my gratitude to Professor Emeritus Trygve E. Eriksen for his support and valuable comments on this work. I am also grateful to Susanna Wold for her comments on this thesis.

Dr. Marcus Amme and Reijo Pehrman - thank you for a fruitful cooperation and a pleasant stay in Karlsruhe.

I would like to thank all present and former co-workers at Nuclear Chemistry for creating a nice atmosphere and making it a pleasure to come to work. In particular I would like to thank;

Ella Ekeroth, for bringing me to Nuclear Chemistry in the first place and for your support and friendship ever since.

Mats Jansson, Anders Puranen and Martin Trummer, for support with computers and laboratory equipment, scientific discussions and a lot of fun!

I would like to thank my family and friends for showing interest in my work and always believing in me. Mum, Dad and Martin – thank you for all your love and support.

SKB is gratefully acknowledged for financial support.

References

1. *Systemanalys - KBS 3-systemet - beskrivning med viktiga vägval under systemets utveckling samt validering av kapseltillverkning och inkapsling Lägesredovisning 2006*, R-06-117, Svensk Kärnbränslehantering AB, 2006
2. SKBF/KBS, *Final Storage of Spent Nuclear Fuel - KBS-3*. 1983, Swedish nuclear fuel supply Co: Stockholm.
3. SKB - Svensk Kärnbränslehantering AB, www.skb.se, 2008
4. L.H. Johnson, D.W. Shoesmith, eds. *Spent Fuel*. in ed. Radioactive wasteforms for the future, ed. W. Lutze and R.C. Ewing. 1988, Elsevier Science Publishers: Amsterdam.
5. D. W. Shoesmith, ed. *The Electrochemistry of Novel Materials*. in ed. Electrochemistry of UO_2 nuclear fuel, ed. J. Lipkowski. 1994, VCH Publishers, Inc.
6. *Deep Repository of Spent Nuclear Fuel SR 97 – Post-closure safety*, TR-99-06, Svensk Kärnbränslehantering AB 1999
7. D. W. Shoesmith, J. Nucl. Mater., 282 (2000) 1-31 and references therein
8. R.L. Segall, R.S.C. Smart, P.S. Turner, eds. *Oxide Surfaces in Solution*. in ed. Surface and Near-Surface Chemistry of Oxide Materials, ed. J. Nowotny and L.-C. Dufour. 1988, Elsevier: Amsterdam.
9. M. Jonsson, F. Nielsen, E. Ekeroth, T. E. Eriksen, Mater. Res. Soc. Symp. Proc. 807 (2004) 385-390
10. B. Grambow, T. Mennecart, M. Fattahi, G. Blondiaux, Radiochim. Acta 92 (2004) 603-609
11. H. Christensen, S. Sunder, Nucl. Technol. 131 (2000) 102-123
12. J. Merino, E. Cera, J. Bruno, J. Quiñones, I. Casas, F. Clarens, J. Giménez, J. de Pablo, M. Rovira, A. Martínez-Esparaza, J. Nucl. Mater. 346 (2005) 40-47
13. O. Roth, M. Jonsson, Cent .Eur. J. Chem. 6 (2008) 1-14
14. G. Choppin, J.O. Liljenzin, J. Rydberg, *Radiochemistry and Nuclear Chemistry*. 1995, Oxford: Reed Educational and Professional Publishing Ltd.
15. J.W.T. Spinks R.J. Woods, *An Introduction to Radiation Chemistry*. Third ed. 1990, New York: John Wiley & Sons Inc.
16. A. Mozunder, *Fundamentals of Radiation Chemistry*. 1999: Academic Press.
17. Smellie, J.A.T., M. Laaksoharju, P. Wikberg, J. Hydrol., 1995. 172: p. 147-169.

18. E. A.B. Ross, B.H.J. Bielski, G.V. Buxton, D.E. Cabelli, C.L. Greenstock, W.P. Helman, R.E. Huie, J. Grodkowski, P. Neta, NDRL/NIST Solution Kinetics Database, 1992 and references therein.
19. J. A. LaVerne L. Tandon, J. Phys. Chem. B 106 (2002) 380-386
20. J. A. LaVerne, S. E. Tonnies, J. Phys. Chem. B 107 (2003) 7277-7280
21. J. A. LaVerne , L. Tandon, J. Phys. Chem. B 107 (2003) 13623-13628
22. J. A. LaVerne J. Phys. Chem. B 109 (2005) 5395-5397
23. J. I. Steinfeld, J.S. Franscisco , W.L. Hase, *Chemical Kinetics and Dynamics*. 2 ed. 1999: Prentice Hall.
24. K. J. Laidler, Chemical Kinetics, Third ed. 1987, New York, Harper & Row and references therein.
25. R.. D. Astumian , Z.A. Schelly, J. Am. Chem. Soc., 106 (1984) 304-308
26. J. Belloni, M. Mostafavi, H. Remita, J.L. Marignier, M.O. Delcourt, New J. Chem. 22 (1998) 1239-1255
27. M.O. Delcourt, J. Belloni, Radiochem. Radioanal. Lett. 13 (1973) 329-338
28. M. Haissinsky, In: J. Dobo, P. Hedvig (Eds), Radiation Chemistry, Akad. Kiado, Budapest, 1972 vol. II pp. 1353-1365
29. A. Henglein Progr. Colloid & Polymer Sci. 73 (1987) 1-3
30. M. A. Nejad , M. Jonsson, J. Nucl. Mater. 334 (2004) 28-34
31. I. Grenthe, D. Ferri, F. Salvatore, G. Riccio, J. Chem. Soc., Dalton Trans., 2439 (1984) 2439-2443
32. M. M. Hossain, E. Ekeroth, M. Jonsson, J. Nucl. Mater. 358 (2006) 202-208
33. M.E. Torrero, E. Baraj, J. De Pablo, J. Giménez , I. Casas, Int. J. Chem. Kinet., 29 (1997) 261 -267
34. S. Sunder, L.K. Strandlund, D.W. Shoesmith, Electrochim. Acta, 43 (1998) 2359 -2372
35. P. Díaz-Arocas, J. Quinones, C. Maffiotte, J. Serrano, J. Garcia, J.R. Almazan, J.Esteban, Mat. Res. Soc. Symp. Proc., 353 (1995) 641 -648
36. J. de Pablo, I. Casas, F. Clarens, F. el Aamrani, M. Rovira, Mat. Res. Soc. Symp. Proc., 663 (2002) 409 -416
37. B. Hanson, B. McNamara, E. Buck, J. Friese, E. Jenson, K. Krupka, B. Arey, Radiochim. Acta, 93 (2005) 159-168
38. M. Amme, Radiochim. Acta, 90 (2002) 399-406
39. M. J. Nicol, C. R. S. Needes, N. P. Finkelstein, In: Leaching Reduct. Hydrometall. A.R. Burkin (Ed.) (IMM, London, 1975) 1-11
40. C. R. S. Needes, M. J. Nicol, N. P. Finkelstein, In: Leaching Reduct. Hydrometall. A.R. Burkin (Ed.) (IMM, London, 1975) 12-19
41. D. W. Shoesmith, S. Sunder, Atomic Energy of Canada Limited, (1991), AECL-10488.

42. E. Ekeroth, M. Jonsson, J. Nucl. Mater., 322 (2003) 242-248
43. L. E. Eary, L. M. Cathles, Metall. Trans. B, 14B (1983) 325-334
44. D. W. Shoesmith, S. Sunder, L.H. Johnson, M.G. Bailey, Mater. Res. Soc. Symp. Proc., 50 (1986) 309-316
45. J. de Pablo, I. Casas, J. Giménez, M. Molera, M. Rovira, L. Duro, J. Bruno Geochim. Cosmochim. Ac., 63 (1999) 3097-3103
46. F. Nielsen, M. Jonsson, J. Nucl. Mater. 359 (2006) 1-7
47. P. Carbol, J. Cobos-Sabathe, J.-P. Glatz, C. Ronchi, V. Rondinella, D.H. Wegen, T. Wiss, A. Loida, V. Metz, B. Kienzler, K. Spahiu, B. Grambow, J. Quiñones, A.M.E. Valiente, SKB Technical Report TR-05-09, 2005
48. E. Cera, J. Bruno, L. Duro, T.E. Eriksen, SKB Technical Report TR-06-07, 2006
49. M. E. Broczkowski, J. J. Noël, D. W. Shoesmith, J. Nucl. Mater., 346 (2005) 16-23
50. H. Kleykamp, J. Nucl. Mater. 374 (2008) 290-292
51. S. Nilsson, M. Jonsson, J. Nucl. Mater. 372 (2008) 160–163
52. M. Trummer, S. Nilsson, M. Jonsson, J. Nucl. Mater. 378 (2008) 55–59
53. T. E. Eriksen, M. Jonsson, J. Merino J. Nucl. Mater. 375 (2008) 331–339
54. F. Nielsen, E. Ekeroth, T. E. Eriksen, M. Jonsson, J. Nucl. Mater. 374 (2008) 286–289
55. J. Soullard, J. Nucl. Mater., 135 (1985) 190-196.
56. H. Matzke, H. Blank, M. Coquerelle, K. Lassmann, I. L. F. Ray, C. Ronchi, C. T. Walker, J. Nucl. Mater., 166 (1989) 165-178.
57. H. Matzke, J. Nucl. Mater., 189 (1992) 141-148.
58. R. K. Willardson, J. W. Moody, H. L. Goering, J. Inorg. Nucl. Chem., 6 (1958) 19-33.
59. W. H. Hocking, D. W. Shoesmith, J. S. Betteridge, J. Nucl. Mater., 190 (1992) 36-45.
60. H. He, P. G. Keech, M. E. Broczkowski, J. J. Noël, D. W. Shoesmith, Can. J. Chemistry 85 (2007) 702-713
61. J. Bruno, E. Cera, M. Grivé, U-B. Eklund T. Eriksen, SKB Technical Report TR-99-26, 1999
62. J. Bruno, E. Cera, M. Grivé, L. Duro, T. Eriksen, SKB Technical Report TR-03-03, 2003
63. M. Vladimirova, D. Fedoseev, M. Dunaeva, Radiochemistry, 44 (2002) 498-500
64. J. Katz, G. Seaborg, L. Morss, *Summary and Comparative Aspects of the Actinide Elements*, in: J. Katz, G. Seaborg, L. Morss (Eds.), The

Chemistry of the Actinide Elements vol. 2, 2nd Ed., Chapman and Hall, London, 1986, pp. 1121-1195
65. S. Ahrland, *Solution Chemistry and Kinetics of Ionic Reactions*, in: J. Katz, G. Seaborg, L. Morss (Eds.), The Chemistry of the Actinide Elements vol. 2, 2nd Ed., Chapman and Hall, London, 1986, pp. 1480-1546
66. C. Musikas, Radiochem. Radioa. Let., 7 (1971) 375-379
67. R.F. Leininger, J.P. Hunt, D.E. Jr. Koshland, Composition and thermal decomposition of uranyl peroxide. U.S. At. Energy Comm. (1958), TID-5290 (Book 2), 704-21
68. E.C. Buck, B.D. Hanson, B.K. McNamara, Geological Society Special Publication 236 (Energy, Waste and the Environment: A Geochemical Perspective) (2004) 65-88
69. J. C. Robbins, CIM Bulletin 71 (1978) 61-67.
70. I. K. Kressin, Anal. Chem. 56 (1984) 2269-2271.
71. S. B. Savvin, Talanta 8 (1961) 673-685.
72. W.A. Patrick, H.B. Wagner, Anal. Chem., 21 (1949) 1279-1280
73. T.C.J. Ovenston, W.T. Rees, Analyst, 75, (1950), 204-208
74. Y. Nimura, K. Itagaki, K. Nanba, Nippon Suisan Gakk., 58, (1992), 1129-1137
75. H. Bader, V. Sturzenegger, J. Hoigne, Water Res., 22 (1988) 1109-1115
76. M. Amme, J. Svedkauskaite, W. Bors, M. Murray, J. Merino, Radiochim. Acta, 95 (2007) 683-692
77. J.A. Schramke, R. Díianpat, R.W. Fulton, G.R. Choppin, J. Radioanal. Nucl. Chem., 130 (1989) 333-346
78. P.A. Bertrand, G.A. Choppin, Radiochim. Acta, 31 (1982) 135-137
79. P. Wardman, J. Phys. Chem. Ref. Data 18 (1989) 1637-1755
80. R.E. Huie, C.L. Clifton, Radiat. Phys. Chem 38 (1991) 477-481
81. M.B. Carver, D.V. Hanley, K.R. Chaplin, MAKSIMA-CHEMIST a program for mass action kinetics simulation by automatic chemical equation manipulation and integration using stiff techniques, Atomic Energy of Canada Limited –Chalk River Nuclear Laboratories, Ontario, 1979.
82. I. Casas, J. Giménez, V. Marti, M.E. Torrero, J. de Pablo, Mater. Res. Soc. Symp. Proc. 294 (1993) 61-66
83. Janata, M. Kelm, B.G. Ershov, Rad. Phys. Chem. 63 (2002) 157-160
84. J. Pucheault, C. Ferradini, R. Julien, A. Deysine, L. Gilles, M. Moreau J. Phys. Chem. 83 (1979) 330-336
85. D. W. King, H. A. Lounsbury, F. J. Millero, Environ. Sci. Technol. 29 (1995) 818-824
86. F. Nielsen, K. Lundahl, M. Jonsson, Journal of Nuclear Materials 372 (2008) 32–35

87. D. Hayes, O.I. Mićić, M.T. Nenadović, V. Swayambunathan, D. Meisel, J. Phys. Chem., 93, (1989), 4603-4609
88. M. Mostafavi, Y. Liu, P. Pernot, J. Belloni, Radiat. Phys. Chem., 59, (2000), 49-51
89. A.H. Souici, N. Keghouche, J.A. Delaire, H. Remita, M. Mostafavi, Chem. Phys. Lett., 422, (2006), 25-29
90. Dzięgielewski, J. Kaleciński, B. Jeżowska-Trzebiatowska, B. Acad. Pol. Sci-Chim., 12, (1964), 537-544
91. J. Dzięgielewski, J. Kaleciński, B. Jeżowska-Trzebiatowska, B. Acad. Pol. Sci-Chim., 12, (1964), 545-549
92. J. Dzięgielewski, J. Kaleciński, B. Acad. Pol. Sci-Chim., 17, (1969), 233-238
93. J. Dzięgielewski, B. Jeżowska-Trzebiatowska, J. Kaleciński, B. Acad. Pol. Sci-Chim., 17, (1969), 239-244
94. J. Belloni, Catal. Today, 113, (2006), 141 and references therein
95. M. Olsson, A-M. Jakobsson, Y. Albinsson, J. Colloid Interf. Sci. , 256, (2002), 256-261
96. A. Hiroki, J. A. LaVerne, J. Phys. Chem., 109, (2005), 3364-3370
97. T. Mennecart, B. Grambow, M. Fattahi, G. Blondiaux, Z. Andriambololona, Mat. Res. Soc. Symp. Proc., 807, (2004), 403-408
98. T. Mennecart, B. Grambow, M. Fattahi, Z. Andriambololona, Radiochim. Acta, 92, (2004), 611-615
99. C. Jégou, V. Broudic, A. Poulesquen, J.M. Bart, Mat. Res. Soc. Symp. Proc., 807, (2004), 391-396
100. S. Stroes-Gascoyne, F. King, J.S. Betteridge, F. Garisto, Radiochim. Acta, 90, (2002), 603-609
101. X-Y. Yu, J. Phys. Chem. Ref. Data, 33 (2004) 747-763

Appendix 1

Reactions and rate constants used in numerical simulations by MAKSIMA-Chemist [81]. Data collected from [18] unless otherwise stated.

Reaction									k (M^{-1} s^{-1})
$OH^{\bullet}$	+	$OH^{\bullet}$	→	H_2O_2					4.0×10^{9}
$OH^{\bullet}$	+	e_{aq}^{-}	→	OH^{-}	+	H_2O			2.0×10^{10}
$OH^{\bullet}$	+	$H^{\bullet}$	→	H_2O					2.5×10^{10}
$OH^{\bullet}$	+	$O_2^{\bullet-}$	→	OH^{-}	+	O_2			1.0×10^{10}
$OH^{\bullet}$	+	H_2O_2	→	H_2O	+	$O_2^{\bullet-}$	+	H^{+}	2.3×10^{7}
$OH^{\bullet}$	+	H_2	→	H_2O	+	$H^{\bullet}$			4.0×10^{7}
e_{aq}^{-}	+	e_{aq}^{-}	→	OH^{-}	+	OH^{-}	+	H_2	5.0×10^{9}
e_{aq}^{-}	+	$H^{\bullet}$	→	OH^{-}	+	H_2			2.0×10^{10}
e_{aq}^{-}	+	$HO_2^{\bullet}$	→	$HO_2^{\bullet}$	+	H_2O			2.0×10^{10}
e_{aq}^{-}	+	$O_2^{\bullet-}$	→	$HO_2^{\bullet}$	+	OH^{-}			1.2×10^{10}
e_{aq}^{-}	+	H_2O_2	→	$OH^{\bullet}$	+	OH^{-}	+	H_2O	1.6×10^{10}
e_{aq}^{-}	+	H^{+}	→	$H^{\bullet}$	+	H_2O			2.2×10^{10}
e_{aq}^{-}	+	O_2	→	$O_2^{\bullet-}$	+	H_2O			2.0×10^{10}
e_{aq}^{-}	+	H_2O	→	$H^{\bullet}$	+	OH^{-}	+	H_2O	2.0×10^{1}
$H^{\bullet}$	+	$H^{\bullet}$	→	H_2					1.0×10^{10}
$H^{\bullet}$	+	$HO_2^{\bullet}$	→	H_2O_2					2.0×10^{10}
$H^{\bullet}$	+	$O_2^{\bullet-}$	→	HO_2^{-}					2.0×10^{10}
$H^{\bullet}$	+	H_2O_2	→	$OH^{\bullet}$	+	H_2O			6.0×10^{7}
$H^{\bullet}$	+	OH^{-}	→	e_{aq}^{-}					2.0×10^{7}
$H^{\bullet}$	+	O_2	→	$O_2^{\bullet-}$	+	H^{+}			2.0×10^{10}
$HO_2^{\bullet}$			→	$O_2^{\bullet-}$	+	H^{+}			8.0×10^{5}
$HO_2^{\bullet}$	+	$HO_2^{\bullet}$	→	O_2	+	H_2O_2			7.5×10^{5}
$HO_2^{\bullet}$	+	$O_2^{\bullet-}$	→	O_2	+	HO_2^{-}			8.5×10^{7}
$O_2^{\bullet-}$	+	H^{+}	→	$HO_2^{\bullet}$					5.0×10^{10}
H_2O_2	+	OH^{-}	→	HO_2^{-}	+	H_2O			5.0×10^{8}
$HO_2^{\bullet}$	+	H_2O	→	H_2O_2	+	OH^{-}			5.7×10^{4}
H_2O			→	H^{+}	+	OH^{-}			2.6×10^{-5}
H^{+}	+	OH^{-}	→	H_2O	+				1.4×10^{11}
$OH^{\bullet}$	+	CO_3^{2-}	→	$CO_3^{\bullet-}$	+	OH^{-}			4.0×10^{8}
$OH^{\bullet}$	+	HCO_3^{-}	→	$CO_3^{\bullet-}$	+	H_2O			1.5×10^{7}
$O_2^{\bullet-}$	+	$CO_3^{\bullet-}$	→	CO_3^{2-}	+	O_2			3.2×10^{8}
H_2O_2	+	$CO_3^{\bullet-}$	→	CO_3^{2-}	+	$O_2^{\bullet-}$	+	$2\ H^{+}$	4.3×10^{5}
$HO_2^{\bullet}$	+	$CO_3^{\bullet-}$	→	CO_3^{2-}	+	$O_2^{\bullet-}$	+	H^{+}	3.0×10^{7}

H^+	+	HCO_3^-	→	CO_2	+	H_2O			1.0×10^{10}
OH^-	+	HCO_3^-	→	CO_3^{2-}	+	H_2O			1.0×10^{9}
H_2O	+	CO_2	→	HCO_3^-	+	H^+			8.4×10^{1}
H_2O	+	CO_3^{2-}	→	HCO_3^-	+	OH^-			3.8×10^{3}
H_2O	+	CO_4^{2-}	→	CO_3^{2-}	+	H_2O			2.0×10^{-1}
$CO_3^{\bullet-}$	+	$CO_3^{\bullet-}$	→	CO_4^{2-}	+	CO_2			7.0×10^{6}
N_2O	+	e_{aq}^-	→	N_2	+	$OH^\bullet$	+ OH^-		9.6×10^{9}
$O_2^{\bullet-}$	+	$O_2^{\bullet-}$	→	HO_2^-	+	O_2			3.5×10^{-1}
e_{aq}^-	+	$CO_3^{\bullet-}$	→	CO_3^{2-}					1.0×10^{10}
$H^\bullet$	+	$CO_3^{\bullet-}$	→	HCO_3^-					1.0×10^{10}
Fe^{2+}	+	H_2O_2	→	Fe^{3+}	+	$OH^\bullet$	+ OH^-		$6.9 \times 10^{4‡}$
Fe^{2+}	+	$HO_2^\bullet$	→	Fe^{3+}	+	$HO_2^\bullet$			1.2×10^{6}
Fe^{2+}	+	$O_2^{\bullet-}$	→	Fe^{3+}	+	H_2O_2			1.0×10^{7}
Fe^{2+}	+	OH•	→	Fe^{3+}	+	OH^-			4.3×10^{8}
Fe^{2+}	+	$CO_3^{\bullet-}$	→	Fe^{3+}	+	CO_3^{2-}			4.3×10^{8}
Fe^{3+}	+	H_2O_2	→	Fe^{2+}	+	$HO_2^\bullet$	+ H^+		2.6×10^{-3}
Fe^{3+}	+	$O_2^{\bullet-}$	→	Fe^{2+}	+	O_2			1.5×10^{8}
Fe^{3+}	+	$HO_2^\bullet$	→	Fe^{2+}	+	H^+	+ O_2		3.1×10^{5}
Fe^{3+}	+	e_{aq}^-	→	Fe^{2+}					6.0×10^{10}
Fe^{3+}	+	$H^\bullet$	→	Fe^{2+}	+	H^+			2.0×10^{5}
$OH^\bullet$	+	Cl^-	→	$ClOH^-$					3.0×10^{9}
$ClOH^{\bullet-}$			→	$OH^\bullet$	+	Cl^-			$6.0 \times 10^{9*}$
$ClOH^{\bullet-}$	+	Cl^-	→	$Cl_2^{\bullet-}$	+	OH^-			1.0×10^{4}
$Cl_2^{\bullet-}$	+	OH^-	→	ClOH-	+	Cl^-			4.5×10^{7}
$Cl_2^{\bullet-}$			→	$Cl^\bullet$	+	Cl^-			$5.7 \times 10^{4*}$
$Cl^\bullet$	+	Cl^-	→	$Cl_2^{\bullet-}$					$7.8 \times 10^{9*}$
$Cl^\bullet$	+	H_2O	→	$ClOH^-$	+	H^+			$1.8 \times 10^{5*}$
$ClOH^{\bullet-}$	+	H^+	→	$Cl^\bullet$	+	H_2O			$2.4 \times 10^{10*}$
$Cl_2^{\bullet-}$	+	CO_3^{2-}	→	$CO_3^{\bullet-}$	+	2 Cl^-			$4.0 \times 10^{8*}$
$Cl_2^{\bullet-}$	+	HCO_3^-	→	$CO_3^{\bullet-}$	+	2 Cl^-	+ H^+		$1.5 \times 10^{7*}$
$OH^\bullet$	+	$H_3C\text{-}CHOH\text{-}CH_3$	→	$(CH_3)_2\text{-}C^\bullet OH$			+ H_2O		1.6×10^{9}
O_2	+	$(CH_3)_2\text{-}C^\bullet OH$	→	$(CH_3)_2C(OH)OO^\bullet$			+ $O_2^{\bullet-}$		4.2×10^{9}
$OH^\bullet$	+	$(CH_3)_2\text{-}C^\bullet OH$	→	CH_3COCH_3			+ H_2O	+ $OH^\bullet$	7.0×10^{5}

‡[85], *[101]